Semi-analytical solution for three-dimensional underwater acoustic propagation from a directional source

Tengjiao He[a,b,*], Shiqi Mo[c], Xin Qing[c]

[a]*Key Laboratory of Marine Intelligent Equipment and System, Ministry of Education, Shanghai Jiao Tong University, Shanghai, 200240, P. R. China*
[b]*School of Mechanical and Aerospace Engineering, Nanyang Technological University, Singapore, 639798, Singapore*
[c]*College of Underwater Acoustic Engineering, Harbin Engineering Univeristy, Harbin, 150040, P. R. China*

Abstract

This article presents a semi-analytical solution for 3D underwater acoustic propagation from a directional source within the framework of adiabatic normal modes. The solution is derived from a double-summation expression provided by the adiabatic mode model using the Fraunhofer far-field approximation and Taylor series expansions to simplify the source-strength integral for directional radiation from a complex source. The derived solution is validated through comparisons with a 2D normal mode code for a directional source in a Pekeris waveguide. Two additional examples highlight the solution's effectiveness in complex engineering problems, including directional propagation under moving internal wave conditions and underwater radiated noise from a vessel near Long Island Sound. A key advantage of this method lies in its semi-analytical formulation, which reduces the process of incorporating source directivity into 3D underwater acoustic propagation to a single propagation model run. Even in fully 3D scenarios, when the transverse eigenfunctions of vertical modal coefficients are coupled, the Dirichlet-to-Neumann operator representing the radiation condition can be stored and reused if the directional source term changes. This improves computational efficiency and reduces numerical costs. Furthermore, the method's full-angle propagation capability ensures an accurate description of the detailed characteristics of complex sources.

Keywords: three dimensional, underwater acoustic propagation, directivity, complex source, semi-analytical formulation

1. Introduction

The modeling of three-dimensional (3D) underwater acoustic propagation is crucial for mitigating underwater noise, exploring marine resources, and evaluating sonar performance. Various approaches are employed to solve 3D underwater acoustic propagation, including normal modes [1, 2], ray tracing [3, 4], parabolic equations [5–10], and fully numerical methods such as the finite element (FE) [11], finite difference [12], spectral element [13, 14], and boundary integral methods [15, 16]. To accurately estimate acoustic emissions from anthropogenic noise sources in realistic marine environments, both the source characteristics and sound propagation must be modeled in detail, as they are inherently integrated in 3D environments. Most of the methods above primarily address problems involving omnidirectional sources [17]. However, anthropogenic noise sources, such as surface vessels and underwater vehicles, are often directional. The incorporation of source directivity into 3D underwater acoustic propagation models remains an open problem. A key focus for future research will be the development of an efficient method with acceptable accuracy to address this practical engineering challenge.

Generally, one can calculate 3D underwater acoustic propagation from a directional source by straightforwardly integrating the results from monopole point sources placed at different spatial positions [18], the fields of which can be given by the existing approaches described above. However, this approach involves extensive numerical operations for point-source integration, which can lead to impractical computation times. The parabolic equation (PE) model can model 3D wave propagation from directional sources by defining an appropriate initial field [14]. However, determining initial fields for complex sources remains challenging, particularly in deep-water environments, as additional numerical treatments are required. Additionally, angular restrictions inherent to the PE method may lead to inaccuracies in representing source characteristics, especially for directions approaching $\pm 90\circ$.

---

*Corresponding author
Email address: hetengjiao@sjtu.edu.cn (Tengjiao He)

When sound waves propagating at these angles are horizontally refracted, predictions based on a limited propagation angle can significantly deviate from observations [19, 20]. The ray method theoretically accounts for source directivity by weighting ray amplitudes according to grazing angles. However, widely used ray models like BELLHOP [21] only consider the in-phase directional beam emitted by complex sources, discarding phase information. An alternative approach involves integrating results from ray models for multiple point sources distributed spatially, as demonstrated in studies modeling acoustic vortices [22, 23]. Nevertheless, this strategy necessitates repeated model implementations, thereby increasing computational complexity. Another approach to addressing this issue is to use fully numerical methods, such as the finite element method (FEM) and the equivalent source method (ESM) [24–26]. Since the FEM is based on volume discretization, the computational domain size is constrained by the acoustic wavelength in 3D problems. This results in a significant demand for computational resources when applying the FEM to large-scale 3D underwater acoustic propagation. Recent studies have demonstrated the ability of the ESM to simulate radiation from a vibrating elastic shell in the presence of double seamounts [27]. While the ESM can integrate structural acoustic radiation with 3D sound propagation, its numerical efficiency remains a major concern, limiting its application in practical engineering problems.

Recent research has demonstrated the computation of a radiated field from a volume source in shallow water using normal mode theory [28, 29]. A key aspect of this method is the decomposition of the sound field into the modal domain, which allows the solution to be expressed as a summation of normal modes with coefficients dependent on the grazing angles modal plane waves. The source-strength integral, which represents radiation from the volume source, can then be simplified, leading to an analytical expression for far-field radiation in the waveguide. The derived solution involves only a single summation of normal modes, avoiding the need for numerical evaluation of the source-strength integral and making it highly efficient for long-range predictions. However, the depth-range variable separation inherent to this solution restricts its validity to a 2D bearing plane, where only the elevation directivity of the source is considered. This excludes the effects of 3D propagation when simulating complex topographies. Despite this limitation, the studies cited above pave the

way for deriving semi-analytical solutions for 3D underwater acoustic propagation from a directional source, provided that the field can be expressed as a modal decomposition. This study aims to develop a 3D underwater acoustic propagation model that incorporates directional sources while maintaining computational efficiency comparable to omnidirectional propagation. To achieve this, we extend existing derivations of modal excitation for complex sources [28, 29] into a fully 3D framework.

The 3D adiabatic mode, an approximate form of 3D coupled normal mode theory, effectively balances computational efficiency and accuracy, making it a suitable candidate for addressing the problem at hand. Previous studies have demonstrated that the 3D adiabatic mode yields promising results in most scenarios where horizontal refraction dominates 3D propagation effects [30, 31]. Furthermore, recent research has introduced a model order reduction (MOR) technique to solve the 3D adiabatic mode [32]. This method expresses the sound field as double summation: one sum represents the modal decomposition over vertical modes, and the other represents the decomposition of the vertical mode coefficient over transverse eigenfunctions. Such a representation is a specific form of the Galerkin method, which employs these eigenfunctions as basis sets. The MOR technique is highly efficient, particularly in longitudinally invariant environments. Moreover, the solution derived from the MOR technique accounts for angles up to ±90∘, enabling an accurate description of source characteristics throughout the entire spatial domain.

The primary contribution of this study is the derivation of a semi-analytical solution for 3D directional underwater acoustic propagation using a reduced-order adiabatic mode framework. By expressing the sound field as a superposition of vertical modes and horizontal eigenfunctions, the proposed model enables directional propagation while maintains computational efficiency equivalent to omnidirectional scenarios. This efficiency is achieved through the use of analytical excitations of modes and eigenfunctions derived from the Huygens integral. The resulting framework provides a practical numerical tool for assessing shipping noise impacts on marine ecosystems. While the current theory excludes modal interactions, addressing these limitations will constitute a focus of future work.

The remainder of this paper is organized as follows. Section 2 presents the formulas for

the proposed theory. Section 3 presents numerical simulations, including validation cases and two application examples. Finally, conclusions are drawn in Section. 4.

2. 3D adiabatic normal mode theory and derivation of modal excitation by directional source

2.1. Order-reduced adiabatic normal modes

This study employs a Cartesian coordinate system where x and y denote the horizontal coordinates, and z represents depth. Within the horizontal plane, x corresponds to the propagation range, while y defines the transverse range. In adiabatic normal mode theory, the transverse range is treated as unbounded, and the depth coordinate z is modeled with a semi-infinite bottom. This coordinate system defines the domain $\mathbb{R}$ as $\mathbb{R} = \mathbb{R}_{x,y} \times \mathbb{R}_z$, where $\mathbb{R}_{x,y} = [0, x_L] \times [y_0, y_L]$ represents the horizontal domain, and $\mathbb{R}_z = [0, \infty]$ specifies the depth domain. Here, x_L and y_L represent the maximal propagation and transverse ranges of interest, respectively, while y_0 is the lower limit in the transverse direction of interest.

2.1.1. Governing equations

We start with the Helmholtz equation governing 3D underwater acoustic propagation [33]:

$$\frac{\partial^2 p}{\partial x^2} + \frac{\partial^2 p}{\partial y^2} + \frac{\partial^2 p}{\partial z^2} + \frac{\omega^2}{c^2(x,y,z)}p = 0, x \in [0, x_L], y \in [y_0, y_L], z \in [0, \infty] \quad (1)$$

where ω is the angular frequency, and the sound pressure $p(x, y, z)$ can be expressed as a truncated expansion over vertical modes:

$$p(x, y, z) = \sum_{j=1}^{\infty} R_j(x, y) P_j(x, y, z), \quad (2)$$

where j specifies the vertical mode number, $R_j(x, y)$ are the modal coefficients, and the orthogonal, vertical modes $P_j(x, y, z)$ can be solved through the Sturm–Liouville problem, given by:

$$\begin{cases} \dfrac{\mathrm{d}^2 P_j}{\mathrm{d}z^2} + \dfrac{\omega^2}{c^2} P_j = k_j^2 P_j, z \in [0, \infty], \\ P_j \Big|_{z=0} = 0, \\ P_j \Big|_{z=z_{sf}^-} = P_j \Big|_{z=z_{sf}^+}, \dfrac{1}{\rho}\dfrac{\mathrm{d}P_j}{\mathrm{d}z}\Big|_{z=z_{sf}^-} = \dfrac{1}{\rho}\dfrac{\mathrm{d}P_j}{\mathrm{d}z}\Big|_{z=z_{sf}^+}. \end{cases} \quad (3)$$

6

In the above equation, k_j are the horizontal modal wavenumbers, and the last two expressions represent the local water/seafloor continuity conditions at $z = z_{sf}(x, y)$ and the pressure-release condition at $z = 0$.

The mode coefficients $R_j(x, y)$ satisfy the coupled equations detailed by Petrov et al. [34]. Dropping the coupling terms gives the adiabatic approximation of the coupled equations and the so-called *horizontal refraction equations* (HREs) is finally derived [35, 36]:

$$\frac{\partial^2 R_j}{\partial x^2} + \frac{\partial^2 R_j}{\partial y^2} + k_j^2(x, y)R_j = 0, x \in [0, x_L], y \in [y_0, y_L]. \tag{4}$$

The boundary conditions for Eq. (4) at $x = x_L$, $y = y_0$, and $y = y_L$ are the radiation conditions at infinity [33], and a source condition should be prescribed at $x = 0$.

2.1.2. Model order reduction using Galerkin-type approximation in horizontal plane

The HREs can be solved using a variety of approaches, including, for example, Gaussian beams [20] and parabolic equations [30]. Instead of using these methods, we introduce a MOR technique to solve these 2D Helmholtz-type equations. This is because the solution provided by the MOR technique covers $\pm 90°$, which is the key to obtaining a correct and detailed description of the sound field produced by a directional source. Another important aspect of this technique is that it analytically expresses the 3D sound field due to an omnidirectional source as a double summation, potentially allowing the derivation of a semi-analytical expression for the directional source. Various numerical aspects of the MOR solution were developed in recent research [32]. The solution involves a decomposition of the coefficients $R_j(x, y)$ over transverse eigenfunctions [33]:

$$R_j(x, y) = \sum_{n=1}^{\infty} S_j^n(x)\phi_j^n(y), \tag{5}$$

where $\phi_j^n(y)$ are the transverse eigenfunctions of $R_j(x, y)$ and $S_j^n(x)$ are their coefficients. The separation of variables in Eq. (5) is equivalent to the integral transform technique for solving the Helmholtz-type equations. The superscript n indicates the order of the transverse eigenfunctions. In essence, the transverse eigenfunctions of $R_j(x, y)$ (orthogonal basis) span an infinite-dimensional space onto which $R_j(x, y)$ are projected. Consequently,

7

the original model, characterized by discretization points along the transverse direction, is reduced to a model represented by the transverse eigenfunctions $\phi_j^n(y)$ (the number of which is typically smaller than the discretization points). Eq. (5) provides a general formulation applicable to bounded domains that support normal mode solutions. This means that there is a waveguide in the horizontal plane. However, in underwater acoustics, the horizontal domain extends infinitely. To resolve this, He et al. [32] introduced two perfectly matched layers (PMLs) to artificially truncate the infinite horizontal domain. This approach allows the eigenproblem associated with $\phi_j^n(y)$ to be closed and solved using a modal projection method (a Galerkin-type approximation in the horizontal plane). Critically, the introduction of PMLs with physical boundaries eliminates the contribution from branch cuts inherent to infinite domains, replacing the continuous spectrum with a summation of high-order modes. Figure 1(a) visualizes the vertical modes P_j and the transverse eigenfunctions ϕ_j^n in the underwater domain for the current analysis.

By reducing the model order of the modal coefficients, the 3D sound pressure can be written as a double summation:

$$p(x, y, z) = \sum_{j=1}^{\infty} \sum_{n=1}^{\infty} S_j^n(x) \phi_j^n(y) P_j(x, y, z) \tag{6}$$

It should be noted that for each vertical mode j, there is a completely independent set of horizontal eigenfunctions, indexed in both j and n.

To derive the expression for the directional source from the MOR solution, we start by assuming longitudinal invariance in the environment. This implies that the waveguide geometries and medium properties (k_j) remain unchanged along the x-axis. This simplification leads to the separation of variables in Eq. (4), indicating that the transverse eigenfunctions $\phi_j^n(y)$ become uncoupled. Considering an omnidirectional point source at (x_0, y_0, z_0) as an excitation, the coefficients of $\phi_j^n(y)$ are reduced to:

$$S_j^n(x) = \frac{\mathrm{i}}{2} \phi_j^n(y_0) \frac{\mathrm{e}^{\mathrm{i}k_{xj}^n(x-x_0)}}{k_{xj}^n} P_j(x_0, y_0, z_0), \tag{7}$$

where k_{xj}^n are the transverse eigenvalues that can be solved through the Sturm–Liouville

problem in the transverse domain:

$$\frac{\mathrm{d}}{\mathrm{d}y}\left[\frac{1}{s(y)}\frac{\mathrm{d}}{\mathrm{d}y}\left(\frac{\phi_j^n}{s(y)}\right)\right]+k_j^2(y)\phi_j^n={k_{xj}^n}^2\phi_j^n, y\in[0,H] \tag{8}$$

where $s(y)$ is introduced due to two PMLs that truncates the infinite transverse domain, and the solution ϕ_j^n is solved subject to the boundary conditions at $y=y_0=0$ and $y=y_L=H$ (H representing the total thickness of the horizontal waveguide, including the two PMLs as illustrated in Fig 1(a) ,and specifically $\hat{\mathbb{R}}_{x,y}=[0,x_L]\times[0,H]$):

$$\phi_j^n(y)\Big|_{y=0,H}=0, \tag{9}$$

It is noteworthy that, while the Sturm-Liouville problem in Eq. (8) implies a bounded horizontal domain, propagation behavior within an unbounded one can be properly modeled by introducing PMLs. Additionally, the source must be positioned between $y=0$ and $y=H$, avoiding placement at the domain boundaries. In a recent study [32], the above eigenproblem was solved through a modal projection method:

$$\begin{cases} \phi_j^n(y)=\sum_{m=1}^N w_j^{m,n}\psi^m(y)=\mathbf{\Psi}^T\mathbf{w}_j^n, \\ \psi^m(y)=\sqrt{\dfrac{2}{H}}\sin\left[\dfrac{m\pi}{H}y\right], \end{cases} \tag{10}$$

where ψ^m denotes the transverse basis modes satisfying Dirichlet boundary conditions at the outer boundaries and forming the orthogonal basis for projecting ϕ_j^n. Here, $w_j^{m,n}$ are the projection coefficients, and $\mathbf{\Psi}$ and $\mathbf{w}_j^n$ represents the vectors of transverse basis modes and projection coefficients, respectively.

To solve the Sturm–Liouville problem in Eq. (8), we first multiply with $s(y)$ and both sides by $\mathbf{\Psi}^T$ and integrate over y from 0 to H. Applying the modal projection from Eq. (10) yields:

$$\left\{\int_0^H s(y)\mathbf{\Psi}^T\frac{\mathrm{d}}{\mathrm{d}y}\left[\frac{1}{s(y)}\frac{\mathrm{d}}{\mathrm{d}y}\left(\frac{1}{s(y)}\right)\right]\mathbf{\Psi}\mathrm{d}y+\int_0^H s(y)k_j^2(y)\mathbf{\Psi}^T\mathbf{\Psi}\mathrm{d}y\right\}\mathbf{W}_j^T={k_{xj}}^2\int_0^H s(y)\mathbf{\Psi}^T\mathbf{\Psi}\mathrm{d}y\mathbf{W}_j^T, \tag{11}$$

where $\mathbf{W}_j$ is the matrix of transverse projection coefficients.

9

Simplifying Eq. (11) yields:

$$\mathbf{\Gamma}_j^{-1}\mathbf{\Upsilon}_j\mathbf{W}_j^T = {k_{xj}}^2\mathbf{W}_j^T, \tag{12}$$

where

$$\mathbf{\Upsilon}_j = \int_0^H \left[-\frac{1}{s(y)}\frac{\partial\mathbf{\Psi}^T}{\partial y}\frac{\partial\mathbf{\Psi}}{\partial y} + k_j^2 s(y)\mathbf{\Psi}^T\mathbf{\Psi} \right]\mathrm{d}y,$$
$$\mathbf{\Gamma}_j = \int_0^H s(y)\mathbf{\Psi}^T\mathbf{\Psi}\mathrm{d}y, \tag{13}$$

and $s(y)$ is given by

$$s(y) = \begin{cases} 1, & d < y < H - d, \\ 1 + \mathrm{i}\sigma(\varepsilon), & \text{otherwise}, \end{cases} \tag{14}$$

with the dimensionless coordinate defined as $\varepsilon = (d - y)/d$ for $0 \leq y \leq d$, and $\varepsilon = (y - H + d)/d$ for $H - d \leq y \leq H$, where d is the PML thickness. Here, σ is the damping function. A quadratic damping function is employed in this study.

Eq. (12) constitutes a generalized matrix eigenvalue problem. The resulting eigenvalues are sorted [37], and their corresponding eigenvectors provide the projection coefficients. The transverse eigenfunction ϕ_j^n is reconstructed via Eq. (10).

The modal summation in Eq. (5) inherently describes discrete spectra. However, open waveguides (e.g., ocean horizontal planes) exhibit continuous spectra due to energy leakage. When propagating transverse eigenfunctions are absent, Eq. (5) becomes inadequate. By truncating the horizontal waveguide with PMLs, this work replaces the continuous spectrum with high-order modes in Eq. (5), effectively closing the eigenproblem. Prior studies, such as [38, 39], validated this approach for atmospheric waveguides, while Barclay and Lin [40] applied analogous horizontal decomposition to 3D underwater acoustics but restricted validity to trapped transverse eigenfunctions via pressure-release boundaries. Our PML-based formulation mimics Sommerfeld radiation conditions through wave attenuation, eliminating this limitation.

2.2. Semi-analytical expression for the directional source term in the longitudinally invariant scenario

To derive the formula for the 3D sound field generated by a directional source using the MOR solution, it is helpful to start with the longitudinally invariant scenario. However,
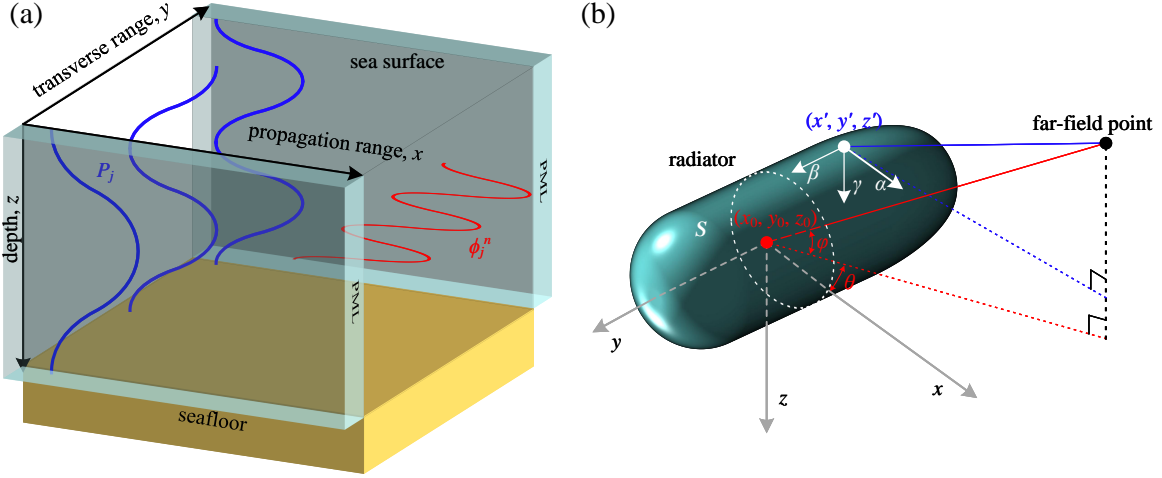
Figure 1: (a) The underwater domain considered in the current analysis, where the vertical modes are represented by blue lines, and the transverse eigenfunction of their coefficients is shown as the red line. (b) The far-field approximation for deriving the semi-analytical expression for a directional source.

the derived expression can be straightforwardly extended to fully 3D cases. This is because the directional source only acts as a modal excitation of $\phi_j^n(y)$ in the local region near the source, which can be considered a longitudinally invariant environment based on the step-size approximation [33]. The coefficients of $\phi_j^n(y)$, which contain the source information, are propagated step-by-step along the longitudinal range through the Dirichlet-to-Neumann (DtN) operator, which depends upon the underwater environment rather than the source.

We begin with an expression for the 3D Green's function with the source placed at (x', y', z') [33]:

$$g(x', y', z'|x, y, z) = \frac{\mathrm{i}}{2} \sum_{j=1}^{\infty} \sum_{n=1}^{\infty} \phi_j^n(y') \frac{\mathrm{e}^{\mathrm{i}k_{xj}^n(x-x')}}{k_{xj}^n} \phi_j^n(y) P_j(x, y, z) P_j(x', y', z'), \qquad (15)$$

As shown in Fig. 1(b), the sound field produced by a volume source whose radiation is directional can be considered as an integration of monopole sources placed on the source surface **S**, given by the equation [18]

$$p_{vol}(x, y, z) = \int_{\mathbf{S}} q(x', y', z') g(x, y, z; x', y', z') \mathrm{d}x' \mathrm{d}y' \mathrm{d}z', \qquad (16)$$

where $q(x', y', z')$ represents the strength of the monopole source.

Substituting Eq. (15) into Eq. (16) and exchanging the order of summation and integration yields

11

$$p_{vol}(x, y, z) = \frac{\mathrm{i}}{2} \sum_{j=1}^{\infty} \sum_{n=1}^{\infty} \frac{1}{k_{xj}^n} \phi_j^n(y) P_j(x, y, z) \int_{\mathbf{S}} q(x', y', z') \phi_j^n(y') \mathrm{e}^{\mathrm{i}k_{xj}^n(x-x')} P_j(x', y', z') \mathrm{d}x' \mathrm{d}y' \mathrm{d}z'.$$

(17)

By expanding the vertical mode P_j and the transverse eigenfunction ϕ_j^n with a Taylor series at the center depth z_0 and at the center transverse position y_0, respectively, the integration in Eq. (17) can be written as

$$A_j = \mathrm{e}^{\mathrm{i}k_{xj}^n(x-x_0)} \int_{\mathbf{S}} q(x_0 + \alpha, y_0 + \beta, z_0 + \gamma) B(\gamma) C(\beta) \mathrm{e}^{-\mathrm{i}k_{xj}^n \alpha} \mathrm{d}\alpha \mathrm{d}\beta \mathrm{d}\gamma,$$

(18)

where

$$B(\gamma) = \sum_{b=0}^{\infty} \frac{1}{b!} \frac{\mathrm{d}^b P_j(x', y', z)}{\mathrm{d}z^b} \bigg|_{z=z_0} \gamma^b$$

(19a)

$$C(\beta) = \sum_{b=0}^{\infty} \frac{1}{b!} \frac{\mathrm{d}^b \phi_j^n(y)}{\mathrm{d}y^b} \bigg|_{y=y_0} \beta^b,$$

(19b)

and the local coordinate of each monopole source is given by

$$\alpha = x' - x_0,$$ (20a)

$$\beta = y' - y_0,$$ (20b)

$$\gamma = z' - z_0.$$ (20c)

The Taylor series can be divided into two parts with odd and even orders. We take $B(\gamma)$ as an example:

$$B(\gamma) = B_o(\gamma) + B_e(\gamma),$$

(21)

where

$$B_o(\gamma) = \sum_{b=0}^{\infty} \frac{1}{(2b+1)!} \frac{\mathrm{d}^{(2b+1)} P_j(x', y', z)}{\mathrm{d}z^{2b+1}} \bigg|_{z=z_0} \gamma^{2b+1},$$ (22a)

$$B_e(\gamma) = \sum_{b=0}^{\infty} \frac{1}{(2b)!} \frac{\mathrm{d}^{(2b)} P_j(x', y', z)}{\mathrm{d}z^{2b}} \bigg|_{z=z_0} \gamma^{2b}.$$ (22b)

12

Next, by neglecting $\mathrm{d}k_{zj}/\mathrm{d}z$ and its higher-order derivatives at the source depth, where $k_{zj} = \sqrt{k^2 - k_j^2}$ is the vertical wavenumber, Eq. (21) can be simplified by reducing the order of derivation of $P_{\mathrm{j}}(z)$ based on Eq. (3):

$$B(\gamma) = \left.\frac{\mathrm{d}P_j(x_0, y_0, z)}{\mathrm{d}z}\right|_{z=z_0} \frac{1}{k_{zj}} \sin(k_{zj}\gamma) + P_j(x_0, y_0, z_0)\cos(k_{zj}\gamma). \tag{23}$$

In the above equation, it is assumed that $P_j(x', y', z_0) \approx P_j(x_0, y_0, z_0)$ because the volume source is significantly smaller in scale compared to the horizontal variations in the medium. The depth-derivative of k_{zj} is neglected because the vertical span of a typical underwater source is on the order of several meters, over which the sound speed exhibits negligible variation.

Similarly, one can simplify $C(\beta)$ by neglecting $\mathrm{d}k_{yj}^n/\mathrm{d}y$ and its higher-order derivatives at the source position, where $k_{yj}^n = \sqrt{k_j^2 - k_{xj}^n{}^2}$, and then using the eigenequation given in Eq. (8). This yields:

$$C(\beta) = \left.\frac{\mathrm{d}\phi_j^n(y)}{\mathrm{d}y}\right|_{y=y_0} \frac{1}{k_{yj}^n} \sin(k_{yj}^n\beta) + \phi_j^n(y_0)\cos(k_{yj}^n\beta), \tag{24}$$

and this holds for most realistic situations, as topography changes minimally over the transverse span of the source.

Therefore, the term of $B(\gamma)$ multiplied by $C(\beta)$ in Eq. (18) can be rewritten as follows:

$$B(\gamma)C(\beta) = E(\gamma, \beta) + F(\gamma, \beta) + K(\gamma, \beta) + L(\gamma, \beta), \tag{25}$$

where

$$E(\gamma, \beta) = \left.\frac{1}{k_{zj}k_{yj}^n}\frac{\mathrm{d}P_j(z)}{\mathrm{d}z}\right|_{z=z_0} \left.\frac{\mathrm{d}\phi_j^n(y)}{\mathrm{d}y}\right|_{y=y_0} \sin(k_{zj}\gamma)\sin(k_{yj}^n\beta) \tag{26a}$$

$$F(\gamma, \beta) = \left.\frac{1}{k_{zj}}\frac{\mathrm{d}P_j(z)}{\mathrm{d}z}\right|_{z=z_0} \phi_j^n(y_0)\sin(k_{zj}\gamma)\cos(k_{yj}^n\beta) \tag{26b}$$

$$K(\gamma, \beta) = \left.\frac{1}{k_{yj}^n}P_j(z_0)\frac{\mathrm{d}\phi_j^n(y)}{\mathrm{d}y}\right|_{y=y_0} \cos(k_{zj}\gamma)\sin(k_{yj}^n\beta), \tag{26c}$$

$$L(\gamma, \beta) = P_j(z_0)\phi_j^n(y_0)\cos(k_{zj}\gamma)\cos(k_{yj}^n\beta). \tag{26d}$$

13

By applying the Euler's formula to the sine and cosine terms in the above equations, the source-strength integration for $E(\gamma, \beta)$ can be further rewritten as

$$E_j^{n'}(y_0, z_0) = \int_{\mathbf{S}} q(\alpha, \beta, \gamma) e^{-ik_{xj}^n \alpha} E(\gamma, \beta) \mathrm{d}\alpha \mathrm{d}\beta \mathrm{d}\gamma$$

$$= -\frac{1}{4k_{zj}k_{yj}^n} \frac{\mathrm{d}P_j(z)}{\mathrm{d}z}\bigg|_{z=z_0} \frac{\mathrm{d}\phi_j^n(y)}{\mathrm{d}y}\bigg|_{y=y_0}$$

$$\int_{\mathbf{S}} q(\alpha, \beta, \gamma) e^{-ik_{xj}^n \alpha} [e^{i(k_{zj}\gamma + k_{yj}^n \beta)} - e^{i(k_{zj}\gamma - k_{yj}^n \beta)} - e^{i(-k_{zj}\gamma + k_{yj}^n \beta)} + e^{i(-k_{zj}\gamma - k_{yj}^n \beta)}] \mathrm{d}\alpha \mathrm{d}\beta \mathrm{d}\gamma$$

$$= -\frac{1}{4k_{zj}k_{yj}^n} \frac{\mathrm{d}P_j(z)}{\mathrm{d}z}\bigg|_{z=z_0} \frac{\mathrm{d}\phi_j^n(y)}{\mathrm{d}y}\bigg|_{y=y_0} [D(\theta_n, \varphi_j) - D(-\theta_n, \varphi_j) - D(\theta_n, -\varphi_j) + D(-\theta_n, -\varphi_j)],$$

$$(27)$$

where $D(\theta, \varphi)$ is the directivity, and, based on the Fraunhofer approximation, $D(\theta, \varphi)$ can be expressed as an integration of the source strength [28, 29],

$$D(\theta, \varphi) = \int_{\mathbf{S}} q(x_0 + \alpha, y_0 + \beta, z_0 + \gamma) e^{ik(\alpha \cos\theta \cos\varphi + \beta \sin\theta \cos\varphi + \gamma \sin\varphi)} \mathrm{d}\alpha \mathrm{d}\beta \mathrm{d}\gamma, \qquad (28)$$

where (θ, φ) is the observation angle.

It should be noted that the simplification in Eq. (27) relies on the following relations:

$$k_{xj}^n = k \cos(\varphi_j) \cos(\theta_n), \qquad (29a)$$

$$k_{yj}^n = k \cos(\varphi_j) \sin(\theta_n), \qquad (29b)$$

$$k_{zj} = k \sin(\varphi_j), \qquad (29c)$$

where φ_j now represents the grazing angle of the up- and down-moving plane wave of the jth vertical mode, and $\theta_n = \mathrm{atan}(k_{yj}^n / k_{xj}^n)$. Using these relations and the formula for directivity given by Eq. (28), the source-strength integrations for $F(\gamma, \beta)$, $K(\gamma, \beta)$, and $L(\gamma, \beta)$ can be reduced to

$$F_j^{n'}(y_0, z_0) = \int_{\mathbf{S}} q(\alpha, \beta, \gamma) e^{-ik_{xj}^n \alpha} F(\gamma, \beta) \mathrm{d}\alpha \mathrm{d}\beta \mathrm{d}\gamma$$

$$= -\frac{i}{4k_{zj}} \frac{\mathrm{d}P_j(z)}{\mathrm{d}z}\bigg|_{z=z_0} \phi_j^n(y_0) [D(\theta_n, \varphi_j) + D(-\theta_n, \varphi_j) - D(\theta_n, -\varphi_j) - D(-\theta_n, -\varphi_j)]$$

$$(30)$$

$$K_j^{n\prime}(y_0, z_0) = \int_{\mathbf{S}} q(\alpha, \beta, \gamma)\mathrm{e}^{-\mathrm{i}k_{xj}^n \alpha} K(\gamma, \beta)\mathrm{d}\alpha\mathrm{d}\beta\mathrm{d}\gamma$$

$$= \frac{1}{4k_{yj}^n} P_j(z_0)\frac{\mathrm{d}\phi_j^n(y)}{\mathrm{d}y}\bigg|_{y=y_0} [D(\theta_n, \varphi_j) - D(-\theta_n, \varphi_j) + D(\theta_n, -\varphi_j) - D(-\theta_n, -\varphi_j)]$$

$$(31)$$

$$L_j^{n\prime}(y_0, z_0) = \int_{\mathbf{S}} q(\alpha, \beta, \gamma)\mathrm{e}^{-\mathrm{i}k_{xj}^n \alpha} L(\gamma, \beta)\mathrm{d}\alpha\mathrm{d}\beta\mathrm{d}\gamma$$

$$\tag{32}$$

$$= \frac{1}{4} P_j(z_0)\phi_j^n(y_0)[D(\theta_n, \varphi_j) + D(-\theta_n, \varphi_j) + D(\theta_n, -\varphi_j) + D(-\theta_n, -\varphi_j)]$$

As a result, the 3D underwater sound propagation from the directional source can be obtained by substituting Eq. (27) and Eqs. (30)–(32) back into Eqs. (17)–(18):

$$p_{vol}(x, y, z) = \frac{\mathrm{i}}{2} \sum_{j=1}^{\infty} \sum_{n=1}^{\infty} \frac{1}{k_{xj}^n} \phi_j^n(y) P_j(x, y, z)\mathrm{e}^{\mathrm{i}k_{xj}^n(x-x_0)}[E_j^{n\prime} + F_j^{n\prime} + K_j^{n\prime} + L_j^{n\prime}] \tag{33}$$

For clarity, after some manipulations of Eq. (33), one can obtain

$$p_{vol}(x, y, z) = \frac{\mathrm{i}}{2} \sum_{j=1}^{\infty} P_j(x, y, z)\left[-\frac{\mathrm{i}}{2k_{zj}}\frac{\mathrm{d}P_j(z)}{\mathrm{d}z}\bigg|_{z=z_0} R_{1j} + \frac{1}{2}P_j(z_0)R_{2j}\right], \tag{34}$$

where

$$R_{1j} = \sum_{n=1}^{\infty} \frac{1}{k_{xj}^n}\phi_j^n(y)\mathrm{e}^{\mathrm{i}k_{xj}^n(x-x_0)}\left[-\frac{\mathrm{i}}{2k_{yj}^n}\frac{\mathrm{d}\phi_j^n(y)}{\mathrm{d}y}\bigg|_{y=y_0} (D_1 - D_2) + \frac{1}{2}\phi_j^n(y_0)(D_1 + D_2)\right] \tag{35a}$$

$$R_{2j} = \sum_{n=1}^{\infty} \frac{1}{k_{xj}^n}\phi_j^n(y)\mathrm{e}^{\mathrm{i}k_{xj}^n(x-x_0)}\left[-\frac{\mathrm{i}}{2k_{yj}^n}\frac{\mathrm{d}\phi_j^n(y)}{\mathrm{d}y}\bigg|_{y=y_0} (D_3 - D_4) + \frac{1}{2}\phi_j^n(y_0)(D_3 + D_4)\right] \tag{35b}$$

In the above equation, D_1, D_2, D_3, and D_4 are given by

$$D_1 = D(\theta_n, \varphi_j) - D(\theta_n, -\varphi_j). \tag{36a}$$

$$D_2 = D(-\theta_n, \varphi_j) - D(-\theta_n, -\varphi_j), \tag{36b}$$

$$D_3 = D(\theta_n, \varphi_j) + D(\theta_n, -\varphi_j), \tag{36c}$$

$$D_4 = D(-\theta_n, \varphi_j) + D(-\theta_n, -\varphi_j). \tag{36d}$$

2.3. Fully 3D situations

The sound field generated by a directional source retains its representation as a double summation over modes via Eq. (34), where each mode's excitation depends on the source directivity. This formulation demonstrates that propagation characteristics are dictated by modes (governed by the ocean environment), while source properties determine the coherent weighting of modal orders through mode excitation. Consequently, Eq. (34) serves as an incident field for the MOR solution in fully 3D scenarios with longitudinal environmental variability [32].

The extension of the MOR solution to fully 3D situations, where the coefficients of $\phi_j^n(y)$ are coupled, is detailed by He et al. [32]. The HRE is first converted into a first-order evolution equation, solved by introducing a Dirichlet-to-Neumann (DtN) operator representing the radiation condition. For R_j, this yields

$$\frac{\partial}{\partial x}\begin{bmatrix} R_j \\ R'_j \end{bmatrix} = \begin{bmatrix} 0 & 1 \\ -(\partial_y^2 + k_j^2) & 0 \end{bmatrix}\begin{bmatrix} R_j \\ R'_j \end{bmatrix}, x \in [0, x_L], y \in [0, H], \tag{37}$$

where $R'_j = \partial_x R_j$. Projecting R_j onto the transverse basis mode ψ^m gives

$$\begin{cases} R_j(x,y) = \sum_{m=1}^{N} a_j^m(x)\psi^m(y), \\ R'_j(x,y) = \sum_{m=1}^{N} a_j^{m\prime}(x)\psi^m(y), \end{cases} \tag{38}$$

with expansion coefficient a_j^m and $a_j^{m\prime}$. Substituting Eq. (38) into Eq. (37) produces

$$\frac{\partial}{\partial x}\begin{bmatrix} \mathbf{a}_j^T \\ \mathbf{a}_j'^T \end{bmatrix} = \begin{bmatrix} \mathbf{0} & \mathbf{I} \\ -\mathbf{\Gamma}_j^{-1}\mathbf{\Upsilon}_j & \mathbf{0} \end{bmatrix}\begin{bmatrix} \mathbf{a}_j^T \\ \mathbf{a}_j'^T \end{bmatrix}, \tag{39}$$

where $\mathbf{a}'_j = \mathbf{Y}_j\mathbf{a}_j$, and $\mathbf{Y}_j$ denotes the admittance matrix (DtN operator) satisfying the governing Riccati equation:

$$\frac{\partial \mathbf{Y}_j}{\partial x} = -\mathbf{\Gamma}_j^{-1}\mathbf{\Upsilon}_j - \mathbf{Y}_j^2. \tag{40}$$

Following [32], we solve Eq. (39) using the second-order Magnus–Möbius scheme. The computation initiates with a back-propagator step .

Eq. (40) is numerically integrated from x_L to x_0 (where the source condition is imposed), with an initial condition of $\mathbf{Y}_j = \mathrm{i}\sqrt{\mathbf{\Gamma}_j^{-1}\mathbf{\Upsilon}_j}$. Operators are stored at each step for reuse

under varying source conditions. Subsequently, forward propagation of $\mathbf{a}_j(x)$ from x_0 to x_L employs these stored operators, with the critical task being the determination of appropriate initial modal excitation $\mathbf{a}_j(x_0)$.

Here, we employ the Magnus method to numerically compute Eq. (40). We assume a uniform discretization of the longitudinal range with a step size of $\Delta x = x_1 - x_0 > 0$. Utilizing the second-order Magnus scheme, Eq. (40) can be expressed in a numerical discretized form:

$$\begin{bmatrix} \mathbf{a}_j(x - \Delta x)^T \\ \mathbf{a}'_j(x - \Delta x)^T \end{bmatrix} = e^{-\Delta x \mathbf{G}[x - (\Delta x/2)]} \begin{bmatrix} \mathbf{a}_j(x)^T \\ \mathbf{a}'_j(x)^T \end{bmatrix}, \tag{41}$$

with

$$\mathbf{G} = \begin{bmatrix} \mathbf{0} & \mathbf{I} \\ -\mathbf{\Gamma}_j^{-1}\mathbf{\Upsilon}_j & \mathbf{0} \end{bmatrix}. \tag{42}$$

The exponential propagator is decomposed into

$$e^{-\Delta x \mathbf{G}[x - (\Delta x/2)]} = \begin{bmatrix} \mathbf{G}_1 & \mathbf{G}_2 \\ \mathbf{G}_3 & \mathbf{G}_4 \end{bmatrix}. \tag{43}$$

The Riccati equation for $\mathbf{Y}_j$ is eventually solved following the Magnus scheme, yielding:

$$\mathbf{Y}_j(x - \Delta x) = [\mathbf{G}_3 + \mathbf{G}_4\mathbf{Y}_j(x)][\mathbf{G}_1 + \mathbf{G}_2\mathbf{Y}_j(x)]^{-1}, \tag{44}$$

and the range-dependent, transverse basis modal coefficients $\mathbf{a}_j(x)$ can be solved using a forward evolutionary procedure:

$$\mathbf{a}_j(x) = \mathbf{M}_j(x)^{-1}\mathbf{a}_j(x - \Delta x), \tag{45}$$

with $\mathbf{M}_j(x) = \mathbf{G}_1 + \mathbf{G}_2\mathbf{Y}_j(x)$.

Next, initial modal excitation $\mathbf{a}_j(x_0)$ for a directional source is determined. Reformulating Eq. (35) as

$$R_{1j}(x_0) = \mathbf{\Phi}_j^T(y)\mathbf{b}_{1j}(x_0), \tag{46a}$$

$$R_{2j}(x_0) = \mathbf{\Phi}_j^T(y)\mathbf{b}_{2j}(x_0). \tag{46b}$$

17

where the transverse eigenfunction coefficients, $\mathbf{b}_{1,2j}$, are defined as

$$\mathbf{b}_{1j}(x_0) = \mathbf{\Lambda}_j(x_0)\mathbf{c}_{1j}(y_0), \tag{47a}$$

$$\mathbf{b}_{2j}(x_0) = \mathbf{\Lambda}_j(x_0)\mathbf{c}_{2j}(y_0). \tag{47b}$$

In the above equation, the diagonal matrix $\mathbf{\Lambda}_j(x_0)$ is given by

$$\mathbf{\Lambda}_j(x_0) = \begin{bmatrix} \dfrac{e^{ik_{xj}^1 x_0}}{k_{xj}^1} & 0 & \cdots & 0 \\[2ex] 0 & \dfrac{e^{ik_{xj}^2 x_0}}{k_{xj}^2} & \cdots & 0 \\[2ex] \vdots & 0 & \ddots & \vdots \\[2ex] 0 & 0 & \cdots & \dfrac{e^{ik_{xj}^N x_0}}{k_{xj}^N} \end{bmatrix}, \tag{48}$$

and the vectors $\mathbf{c}_{1,2j}(y_0)$ are

$$\mathbf{c}_{1j}(y_0) = \frac{1}{2} \begin{bmatrix} -i\dfrac{d\phi_j^1(y)}{dy}\bigg|_{y=y_0} \dfrac{1}{k_{yj}^1}(D_1 - D_2) + \phi_j^1(y_0)(D_1 + D_2) \\[2ex] -i\dfrac{d\phi_j^2(y)}{dy}\bigg|_{y=y_0} \dfrac{1}{k_{yj}^2}(D_1 - D_2) + \phi_j^2(y_0)(D_1 + D_2) \\[2ex] \vdots \\[2ex] -i\dfrac{d\phi_j^N(y)}{dy}\bigg|_{y=y_0} \dfrac{1}{k_{yj}^N}(D_1 - D_2) + \phi_j^N(y_0)(D_1 + D_2) \end{bmatrix}, \tag{49}$$

and

$$\mathbf{c}_{2j}(y_0) = \frac{1}{2} \begin{bmatrix} -i\dfrac{d\phi_j^1(y)}{dy}\bigg|_{y=y_0} \dfrac{1}{k_{yj}^1}(D_3 - D_4) + \phi_j^1(y_0)(D_3 + D_4) \\[2ex] -i\dfrac{d\phi_j^2(y)}{dy}\bigg|_{y=y_0} \dfrac{1}{k_{yj}^2}(D_3 - D_4) + \phi_j^2(y_0)(D_3 + D_4) \\[2ex] \vdots \\[2ex] -i\dfrac{d\phi_j^N(y)}{dy}\bigg|_{y=y_0} \dfrac{1}{k_{yj}^N}(D_3 - D_4) + \phi_j^N(y_0)(D_3 + D_4) \end{bmatrix}. \tag{50}$$

Transforming Φ_j in Eq. (46) into the transverse basis mode Ψ via Eq. (10)

18

$$\mathbf{\Phi}_j^T = \mathbf{\Psi}^T \mathbf{W}_j, \tag{51}$$

and this yields

$$\mathbf{a}_j(x_0) = \mathbf{W}_j \mathbf{b}_j(x_0), \tag{52}$$

By substituting Eq. (47) into Eq. (52), the initial fields $\mathbf{a}_{1,2j}(x_0)$ are obtained, which can then be used as input to Eq. (45).

3. Numerical simulations

3.1. Model validation

The proposed method is validated through a comparison with an N×2D normal mode model, which was developed to predict structural acoustic radiation in a range-independent waveguide [28, 29]. This model incorporates the vertical source directivity into normal mode theory by determining the modal excitation based on the grazing angle at which the corresponding modal plane waves propagate. The azimuthal dependence of the source directivity is accounted for by dividing the directivity function into slices according to the azimuthal angle, with each slice used to weight the modal excitation in its respective range-azimuth bearing plane [29]. Consequently, this model is implemented in cylindrical coordinates rather than Cartesian coordinates. It is important to note that the author intended to validate the proposed theory in an ocean environment with range dependence. However, to the author's knowledge, no benchmark solution currently exists for the specific problem addressed in this article. The only available reference solution is the N×2D normal mode model, which was derived for a range-independent waveguide. Although the benchmark case is presented in a range-independent environment, the proposed theory's ability to incorporate source directivity into the 3D adiabatic mode model can still be validated.

The test scenario considered here is a sound field generated by a source with an analytical directivity given by

$$D(\theta, \phi) = -i \cos\left(2\theta + \frac{\pi}{6}\right)\left[\sin\left(2\theta + \frac{\pi}{6}\right) + 0.25\right] + \sin\left(\theta + \frac{\pi}{6}\right) + 0.55 \cos\left(6\theta + \frac{\pi}{6}\right) \sin\left(6\theta + \frac{\pi}{6}\right). \tag{53}$$

The directivity is shown in Fig. 2.
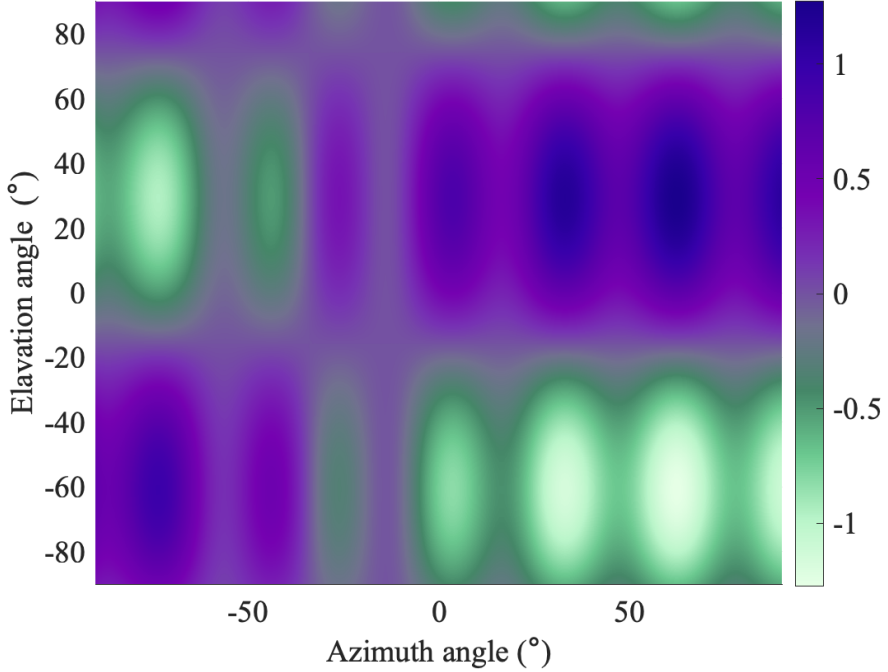
Figure 2: The source directivity considered in the simulation.

The ocean environment is modeled as a Pekeris waveguide, consisting of an iso-velocity water column above a homogeneous seabed. The water depth is 200 m, with a sound speed of 1500 m/s and a density of 1000 kg/m^3. The bottom has a sound speed of 1750 m/s, an attenuation of 0.4 dB/λ, and a density of 1900 kg/m^3. The computational domain spans 8 km $\times$ 2 km, with the directional source located at coordinates (0 km, 1 km, 100 m). Figure 3 provides a schematic of this simulation.

Figures 4 and 5 compare the results with the reference solution obtained from the normal mode model [29] at 100 Hz. The results are shown in the vertical plane at $y = 1$ km (corresponding to $y = 0$ km in cylindrical coordinates for the reference solution) and the horizontal plane at $z = 100$ m. It is important to note that the reference solution is computed in cylindrical coordinates. Despite the different coordinate systems, both solutions show strong agreement in the two planes, particularly in terms of the overall sound pressure level contours and energy distribution. More detailed and convincing comparisons along the lines

20
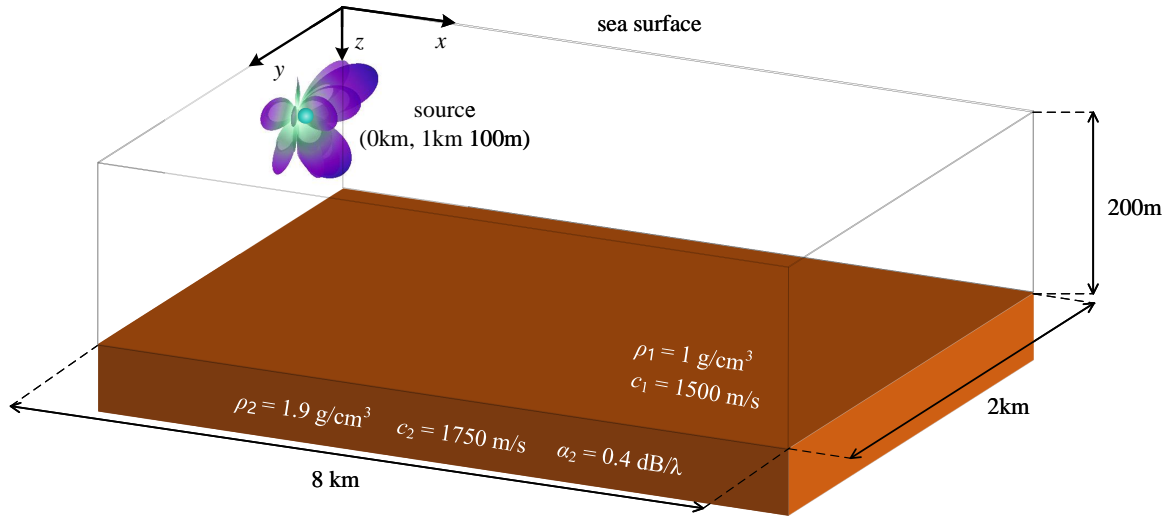
Figure 3: A schematic of the simulation in a Pekeris waveguide, with a source with the directivity shown in Fig. 2.

$y = 1$ km and $x = 1$ km are presented in Fig. 6. The excellent agreement with the reference solution, with errors barely exceeding 1 dB, demonstrates the effectiveness of the proposed theory in incorporating source directivity into the 3D adiabatic mode model.
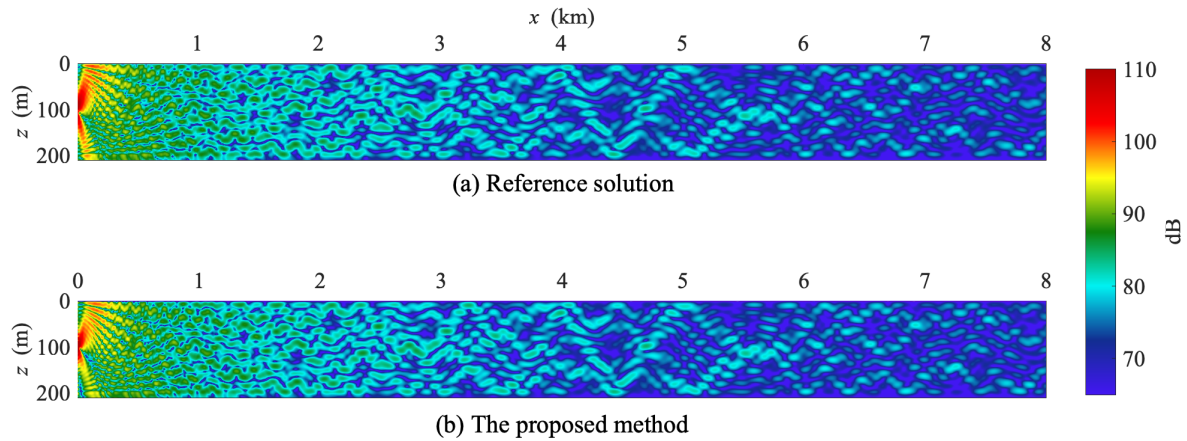
Figure 4: The sound field produced by the directional source in the vertical plane $y = 1$ km ($y = 0$ km for the reference solution) at 100 Hz: (a) the reference solution, and (b) the result calculated by the proposed method.
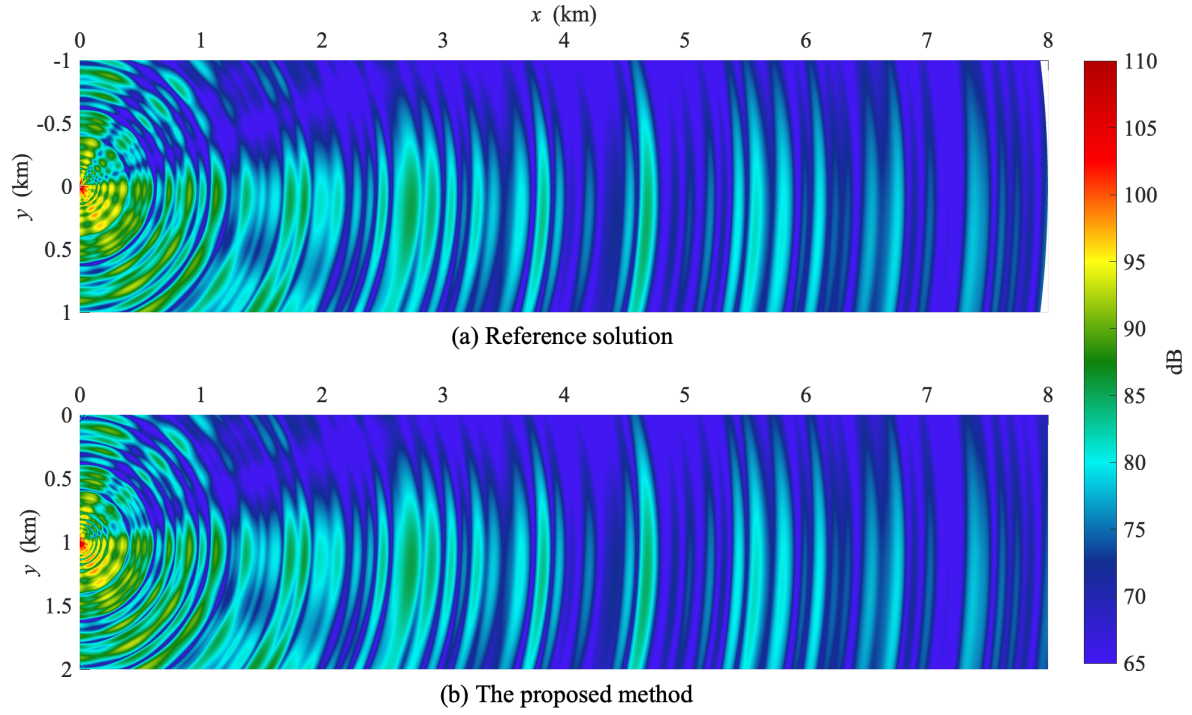
Figure 5: The sound field produced by the directional source in the horizontal plane $z = 100$ m at 100 Hz: (a) the reference solution, (b) the result calculated by the proposed method.
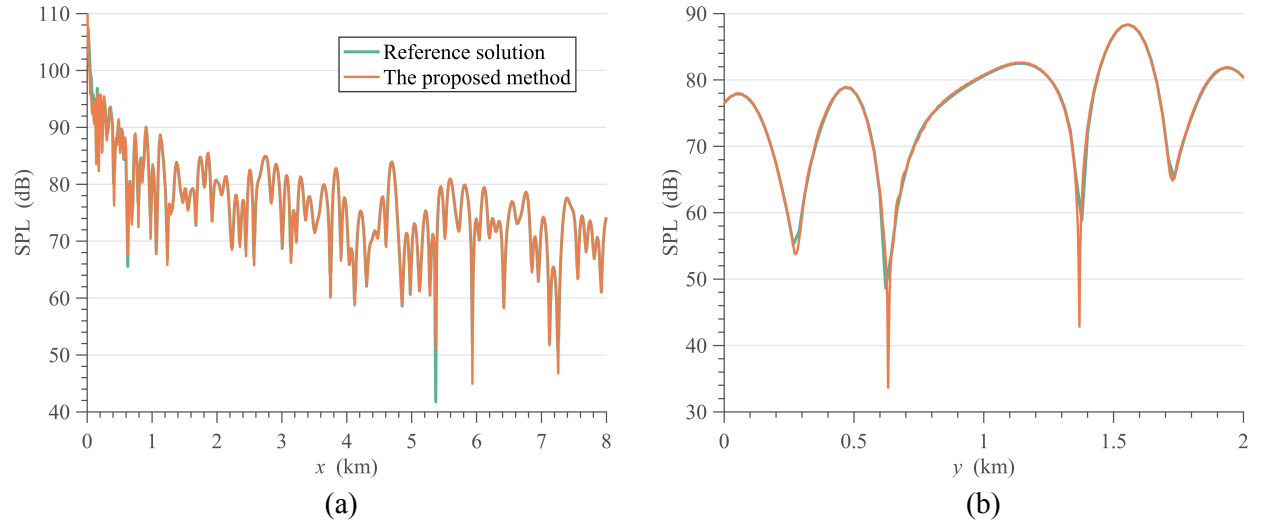
Figure 6: A detailed comparison of the sound pressure levels predicted by the reference solution and the proposed method at 100 Hz: (a) $y = 1$ km and (b) $x = 1$ km.

22

3.2. Application examples

After benchmarking the proposed theory, this section presents two application examples: 3D underwater acoustic propagation from a directional source in an ocean environment with moving internal waves (IWs) and the prediction of underwater radiated noise from a surface vessel in the Long Island Sound region [41]. The first example demonstrates that the proposed theory, under the assumption of transversal symmetry, yields highly promising results that align well with data recorded during the SWARM 95 (shallow-water acoustics in a random medium) experiment [42], highlighting its computational efficiency for a simplified ocean environment. The second example addresses a more realistic scenario. The mechanical noise generated by a surface ship is modeled in detail using the FEM, while bathymetric data from the National Oceanic and Atmospheric Administration (NOAA) [41, 43] dataset is utilized to assess the adverse impact of shipping noise on marine fauna in the Long Island Sound region.

3.2.1. Case 1: 3D underwater acoustic propagation from a directional source in the ocean with moving internal waves

The first example considers the scenario of the SWARM 95 experiment, which was conducted in the New Jersey continental shelf in 1995. Details of the experimental setup and data can be found in previous studies [42, 44, 45]. Here, we summarize the experimental setup from two perspectives: the ocean environment and the measurement configuration.

We consider the underwater environment from 19:00 to 20:00 GMT on 4 August 1995 [45]. The water column is 70 meters thick and consists of three distinct layers. The top and bottom layers are isothermal, with thicknesses of 15 meters and 40 meters, respectively, and corresponding sound speeds of 1530 m/s and 1480 m/s. Between these isothermal layers lies the thermocline, a transition region where the sound speed decreases linearly with depth from 1530 m/s at the top to 1480 m/s at the bottom. The thermocline extends from a depth of 15 meters to 30 meters [46]. The IW train causes fluctuations in the upper and lower boundaries of the thermocline. For simplicity, we assume a model of the IW train moving at a constant speed of 0.65 m/s. The shape of the IW is described by M. Badiey et al.[45]:
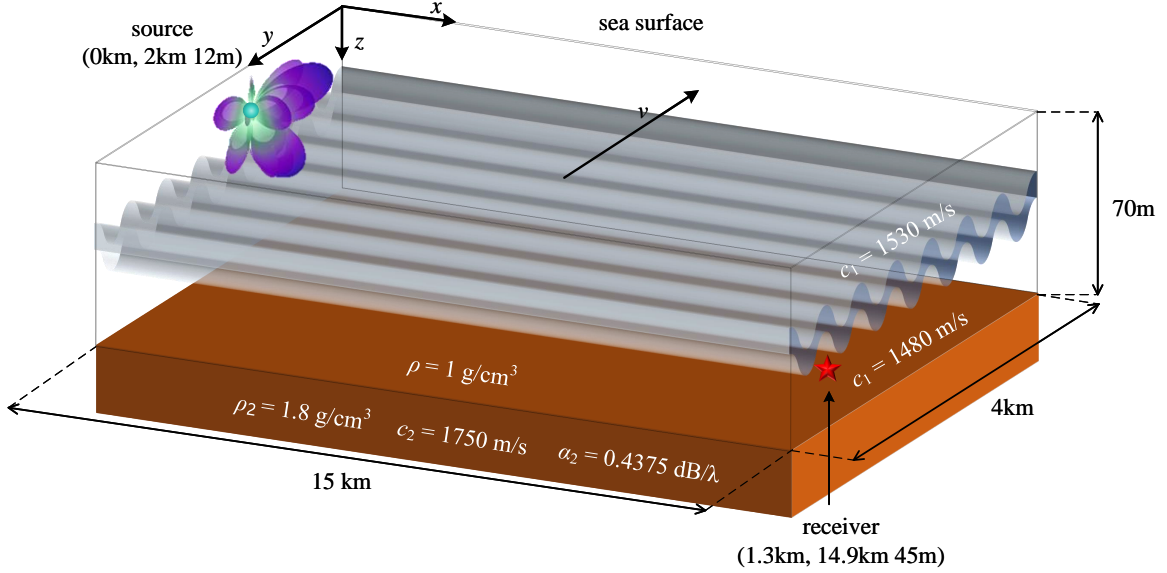
Figure 7: A schematic of the SWARM 95 simulation. The directional source shown in Fig. 2 is considered, and the SWARM 95 experimental scenario is reproduced. The semi-transparent gray waves represent that the IW, described by Eq. (54), moves along the y axis with a constant speed of 0.65 m/s.

$$\text{ISW}(y) = 10\text{sech}^2[(y - 0.65)/70], \tag{54}$$

with the wave moving in the negative y direction, as illustrated in Fig. 5. The seabed has a density of 1800 kg/m^3, a sound speed of 1750 m/s, and an attenuation of 0.4375 dB.

During the experiment, the source was positioned at a depth of 12 m, while the receiver was deployed 15 km from the source, forming a source-receiver line with an oblique angle of 5° relative to the wavefront of the IWs [45]. The receiver was located at a depth of 45 m [46]. The computational domain for the simulation spans 15 km $\times$ 4 km $\times$ 70 m. Figure 7 provides a schematic of the simulation. The same source directivity determined by Eq. (53) was used in this simulation.

Figure 8 shows snapshots of the horizontal sound field for different geotimes at a receiver depth of 45 m. The frequency is set to 60 Hz, corresponding to a peak observed in the acoustic signals used during the SWARM 95 experiment [45, 46]. An uneven energy distribution is evident, caused by both the spatial directivity of the source and sound intensity variations modulated by the movement of IWs. At different geotimes, distinct 3D propagation effects
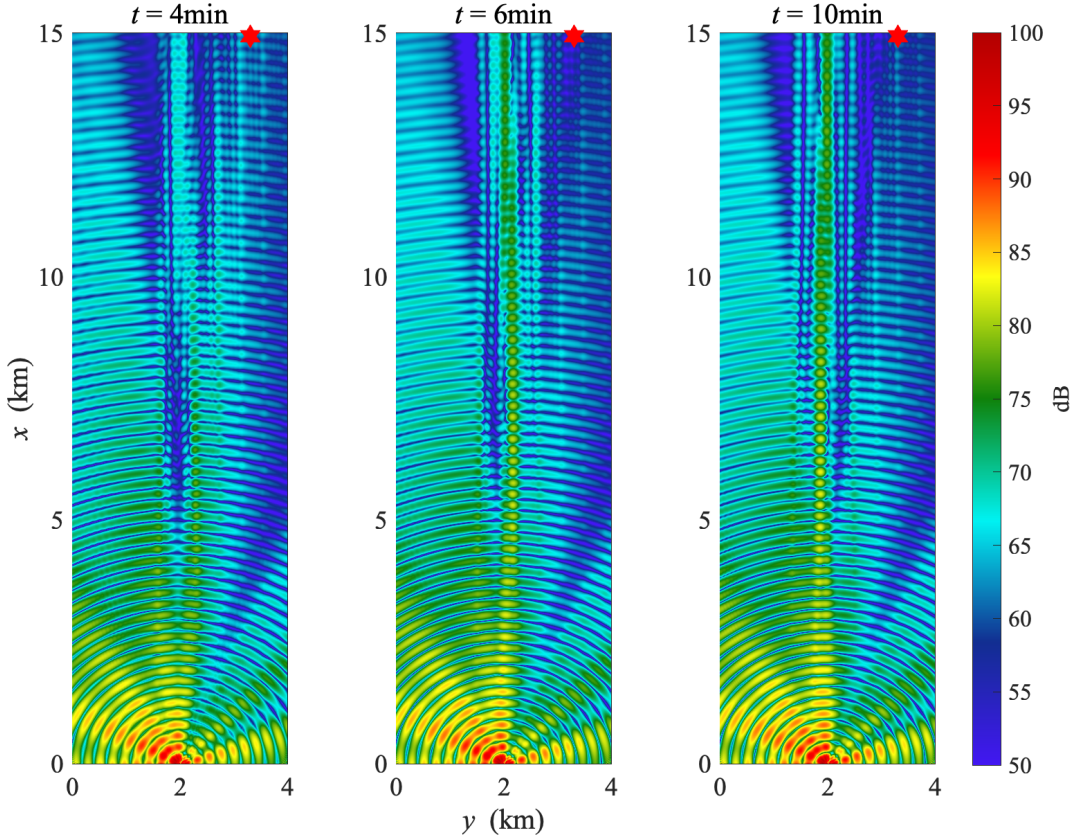
Figure 8: The horizontal sound field due to the directional source at different geotimes. The source frequency is 60 Hz. See the supplementary material SuppPub1 for a complete video demonstrating the 3D sound field at different geotimes.

emerge. At t=4 min, horizontal defocusing is noticeable along the x-axis where the source is positioned, creating a shadow zone around y=2 km. Simultaneously, strong interference is observed at the hydrophone, marked by a red pentagram. This results from energy leakage between two IW crests passing through the hydrophone. At t=6 min, a strong energy path emerges along y=2 km as two wave crests move to either side of the source. Horizontal ducting occurs due to horizontal refraction confined between the IW crests. Defocusing at the hydrophone suggests that one IW crest is directly above it. Horizontal focusing reoccurs at the hydrophone at t=10 min. These results demonstrate clear spatiotemporal variations in the sound intensity due to 3D propagation effects modulated by IWs.

For comparison, we also present results for an omnidirectional point source in Fig. 9.
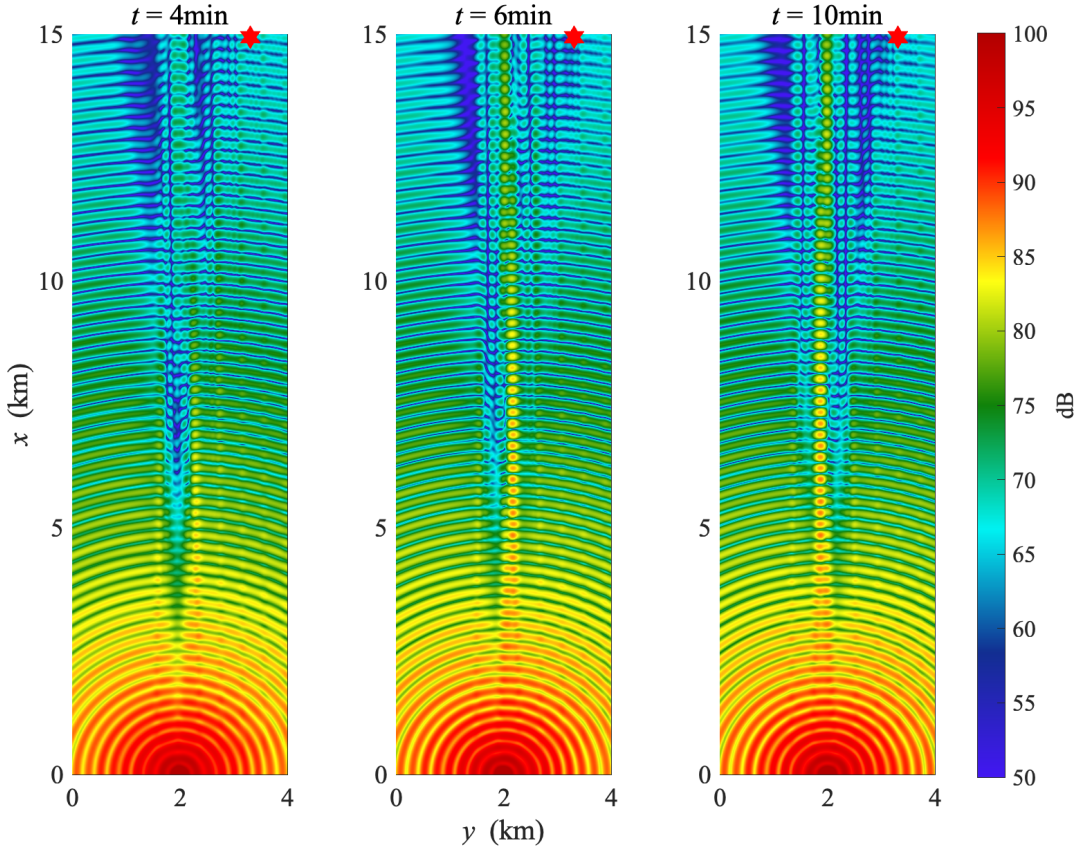
Figure 9: The horizontal sound field due to an omnidirectional source at different geotimes. The source frequency is 60 Hz. See the supplementary material SuppPub2 for a complete video demonstrating the 3D sound field at different geotimes.

Unlike in the directional source case, the uneven energy distribution here is solely due to IW modulation. While similar 3D propagation effects are observed at various stages, the magnitude of the energy fluctuations differs, as the energy distributions in the horizontal plane vary between different sources. Directional radiation locally enhances or diminishes the 3D propagation effects, as these effects depend on the horizontal grazing angle of the incident wave energy. When the directional radiation directs significant energy toward those horizontal angles at which the 3D effect is triggered, the 3D propagation is amplified, and vice versa.

To illustrate this in detail, Fig. 10 compares the normalized sound pressure amplitude recorded between 19:30 and 20:00 GMT. When the source is directional, enhanced ducting
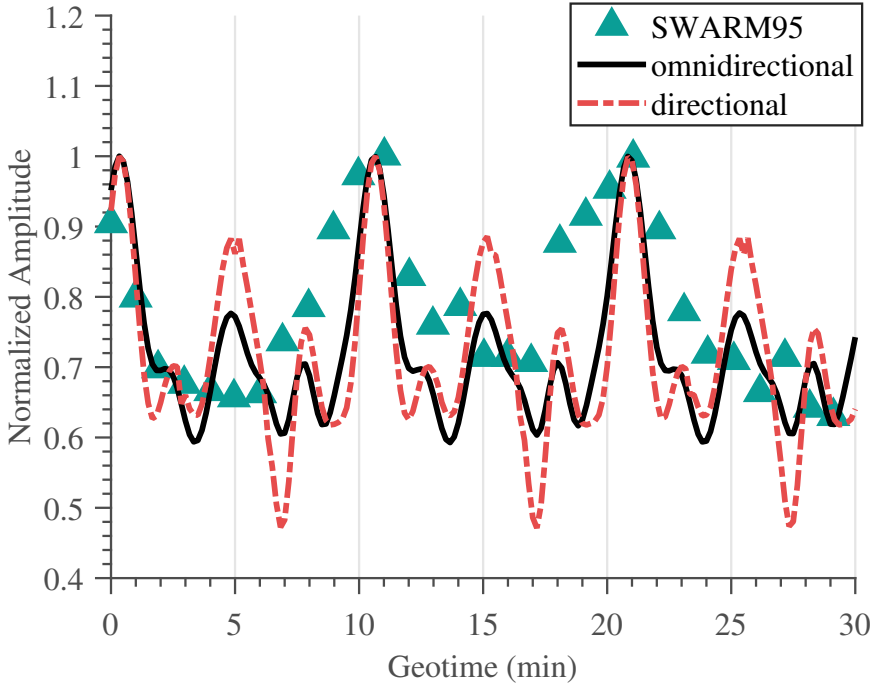
Figure 10: A comparison with the normalized sound pressure amplitude recorded between 19:30 and 20:00 GMT during SWARM 95. The cyan triangles represent the experimental data, and the solid black line and the dashed red line are the predictions of the proposed method using omnidirectional and directional sources, respectively.

is observed at 5 minutes, while horizontal defocusing becomes apparent at 7 minutes. In the directional case, a distinct radiation lobe forms along the line connecting the source and receiver. On either side of this lobe are destructive regions with minimal radiation, allowing any 3D propagation effects originating from this region to be neglected. However, in the omnidirectional case, the uniform radiation from the source compensates for the destructive region, potentially increasing the energy of the horizontal refraction produced by this region. This contributes to the received field at the hydrophone. As a result, the horizontal defocusing observed at 6 minutes is enhanced by the directional source. Despite the differences between the omnidirectional and directional cases, which arise from different modal excitations, both cases exhibit a notable similarity resulting from periodic signal peaks and troughs align with the source position within internal wave ducts. To prove that, the experimental results recorded at the hydrophone are provided by M. Badiey et al.[45].

Notably, these results are the snap shots instead of the entire time-domain signal. The predicted time variation and magnitude of the received sound pressure fluctuations show a qualitative agreement with the experimental field data.

3.2.2. Case 2: Underwater radiated noise from a surface vessel in the shallow water environment of Long Island Sound

The second example presented here involves the modeling of 3D underwater radiated noise from a surface vessel in the shallow waters of Long Island Sound, located off the eastern coast of the United States. Bathymetric data were obtained from the NOAA dataset [43]. Specifically, as shown in Fig. 11, a local topographic section was extracted for the simulation, spanning from 41.23 °N to 41.21 °N in latitude and from 72.1 °W to 72 °W in longitude, covering an area of 8.33 km by 2.36 km. The vessel's horizontal position was set as (0 m, 1.13 km).
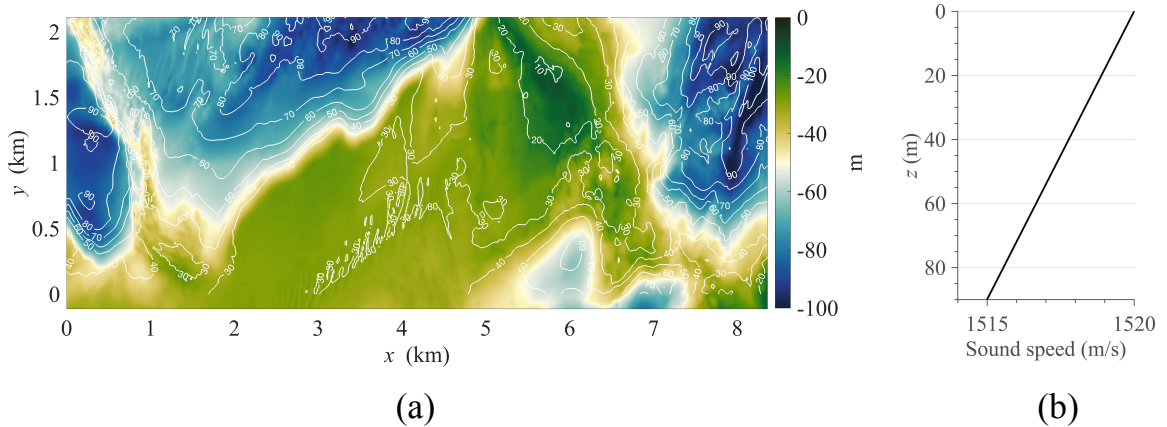

Figure 11: (a) The topography used in the simulation, covering an area of 8.33 km by 2.36 km. The area spans from 41.23 °N to 41.21 °N in latitude and from 72.1 °W to 72 °W in longitude. (b) The sound speed profile used in the simulation.

A weak negative sound speed profile, as observed by T. C. Oliveira et al.[41], was assumed in the water column, with a gradient of -0.0556 m/s^2. The sound speed at the surface ($z = 0$ m) was 1520 m/s, and the water density was set to 1000 kg/m^3. The sandy sediment was modeled with a sound speed of 1700 m/s, a density of 1500 kg/m^3, and an attenuation of 0.5 dB/λ.

The underwater radiated noise considered in this study originated solely from mechanical

28

noise produced by the hull's vibration, driven by a point force. The hull model, extracted from the COMSOL Application Gallery, had a length of 36 m and a beam width of 6 m, as shown in Fig. 12(a). FE modeling was performed to simulate the mechanical noise. The FE simulation setup is depicted in Fig. 12(b)–12(c). A solid-acoustic interaction model was developed, with the ship hull represented by solid mechanics and the surrounding water domain governed by pressure acoustics. An acoustic-solid coupling condition was imposed at the hull-water interface to simulate the vibro-acoustic behavior. The point force was applied at the junction where the propeller penetrates the hull, as shown in Fig. 12(b). The water domain was modeled as a half-space beneath a pressure-release boundary, represented by a hemisphere, with the outer layer treated as a PML. The water domain meshing followed the rule of 1/6 of the wavelength for accuracy, while the solid domain required ten times denser meshing to capture detailed vibro-acoustic behavior [11, 47]. A 10-layer sweep meshing was used for the PML. Additionally, to reduce computational costs, only the left half of the FE model was implemented, utilizing a symmetry condition along the $x = 0$ plane, as shown in Fig. 12(c).

Using the established FE model, Fig. 13 shows the near-field and far-field computations of the simulated mechanical noise at 200 Hz. The far-field results were obtained using the built-in far-field calculation feature in COMSOL. The inner boundary of the PML was set according to the far-field calculation condition, with the integral extending to $r \to \infty$. Apparent directional radiation patterns are observed in both the near-field and far-field results. In the far field, the radiation is essentially a function of the observation angles, denoted as $D(\theta, \varphi)$ in Eq. (30). It should be noted that the direct result from the far-field computation needs to be corrected to compensate for the so-called Lloyd mirror (LM) effect. One of the most convenient ways to recover the free-field radiation of the vessel is to divide the direct far-field result by the far-field expression for the LM pattern [48]:

$$D_{\text{free}}(\theta, \varphi) \approx \frac{D(\theta, \varphi)}{\sin[kd_s \sin \varphi]}, \tag{55}$$

where d_s is the draft depth.
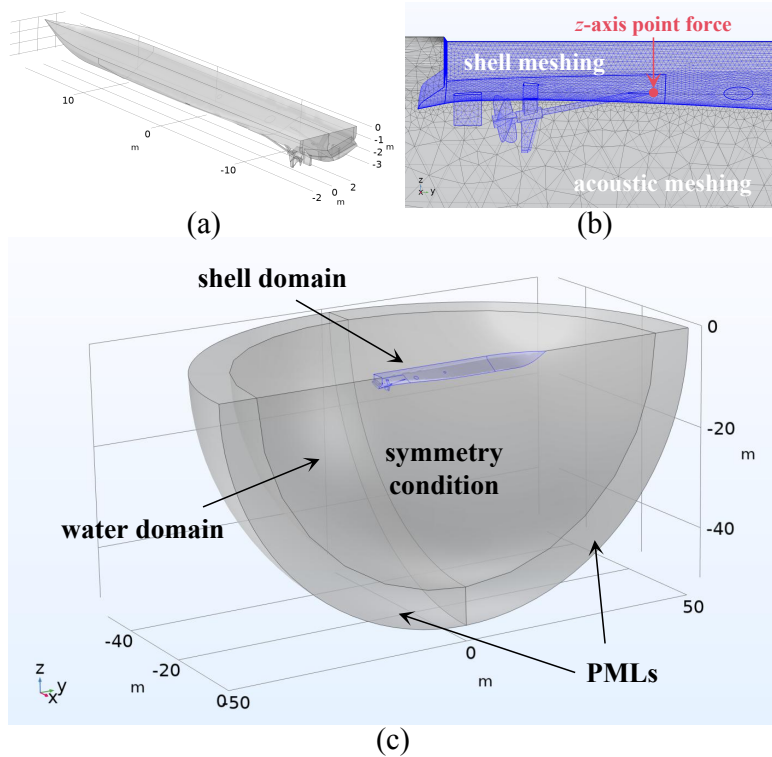
Figure 12: (a) A schematic of the finite element model used to obtain the far-field radiation from a vibrating vessel hull. (b) The detailed meshing used in the region near the hull. (c) The configuration of the semi-half domain where the shell and water domains are coupled together.

The far-field computation, corrected by Eq. (55), serves as the input for the reduced-order adiabatic mode model, facilitating the coupling of directional 3D underwater radiated noise with a 3D underwater environment. In the fully 3D simulation, the transverse eigenfunctions of the vertical modal coefficients are coupled through the DtN operator, which represents the radiation condition along the propagation direction. Once computed, the DtN operator can be stored locally and reused when the source term changes. Equations (28) and (33) together define the initial modal amplitude (or initial field) for the DtN operator, enabling a marching process for propagating the sound field that is significantly faster than assembling the DtN operator itself. This approach is particularly valuable for evaluating different sources in the same underwater environment or the same radiator at varying azimuth angles.

Figure 14 illustrates the 3D sound field generated by a vessel traveling at an oblique angle of 45° with respect to the $x = 0$ m axis at 200 Hz. It showcases a pronounced directional
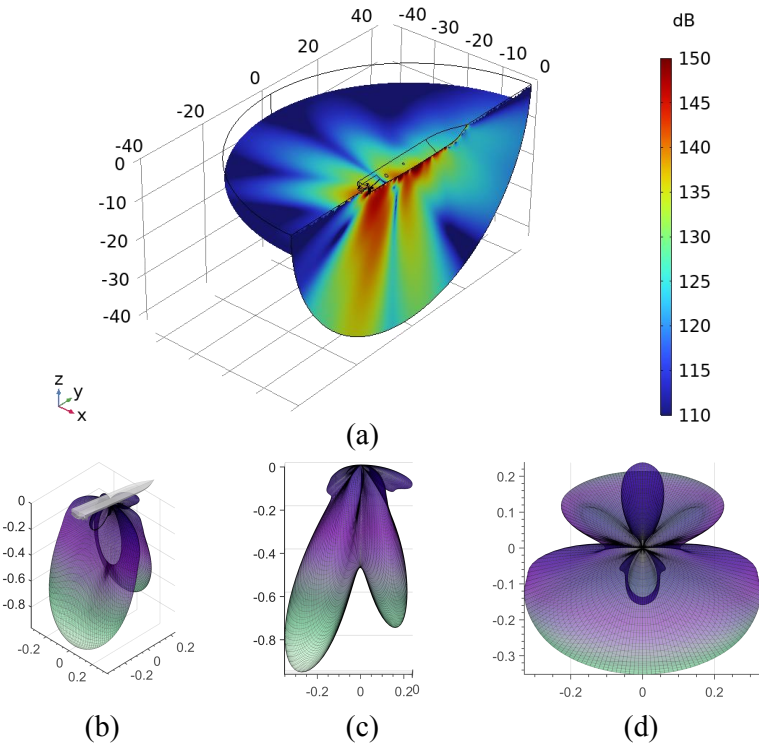
Figure 13: Acoustics radiation from the vessel hull vibrating at 200 Hz, with the far-field results predicted using the far-field calculation module in the COMSOL software. Panels (a) and (b) show the near-field radiation and the dipole-like, far-field radiation, respectively. Panels (c) and (d) show the far-field pattern from the side and top views, respectively.

radiation pattern caused by the vessel hull being driven by a point force. The radiation pattern exhibits strong intensity in the stern direction, as well as a "butterfly-like" beam emitted from the vessel's sides. Significant transmission losses are attributed to the vessel's shallow source depth. In the region where $y < 1$ km and 2 km $< x < 6$ km, a seamount-like topography obstructs propagation along the x-axis, resulting in noticeable horizontal scattering. Consequently, only a small amount of energy is transmitted through this region, as evidenced at a depth of 20 m.

Figure 15 illustrates the 3D sound field generated by the vibrating vessel at $z = 30$ m with different orientation angles. The stern direction is defined as $\theta = 0\circ$ and the bow direction as $\theta = 180\circ$. As the vessel's orientation changes, distinct radiation patterns emerge in both the near and far fields. Radiation from the ship's stern transmits significant energy through the seamount region where $y < 1$ km and 2 km $< x < 6$ km. When the orientation angle
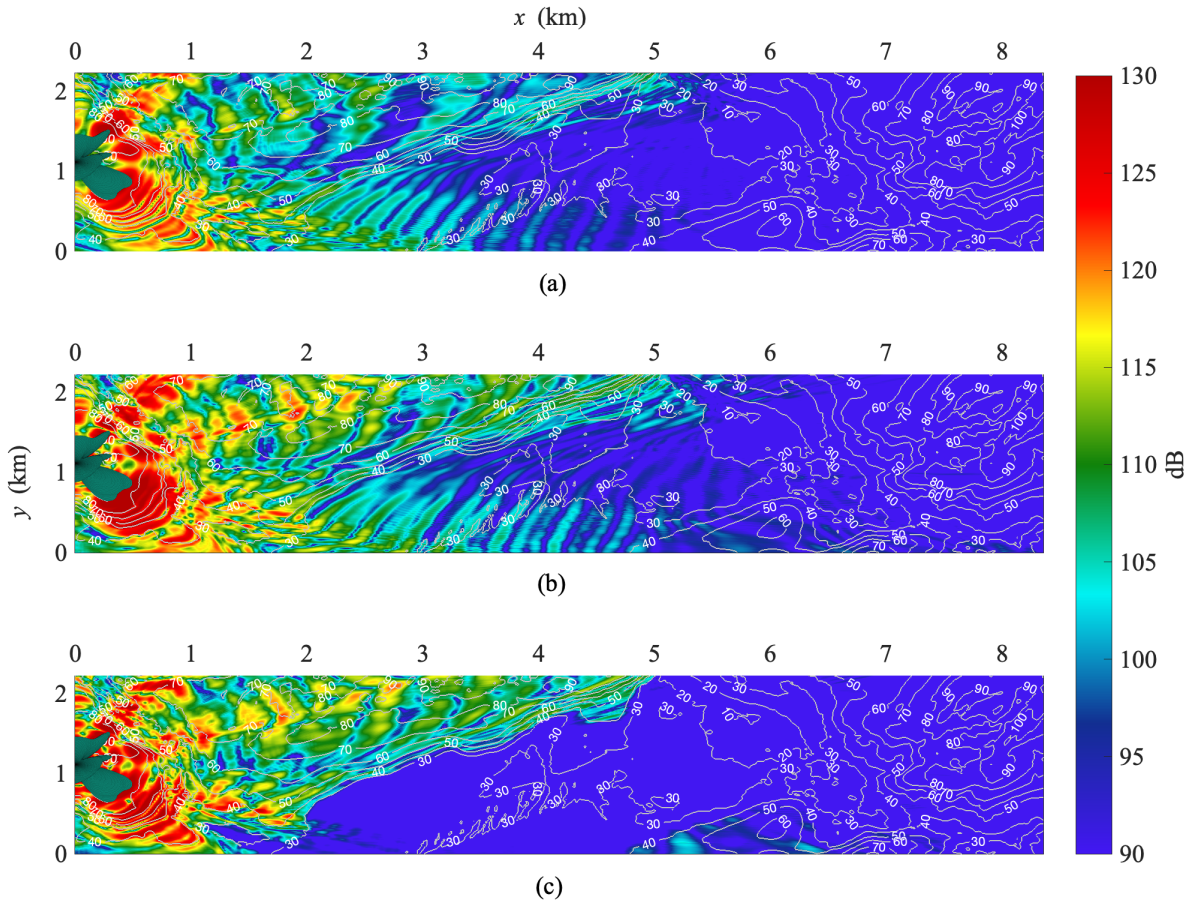
Figure 14: The 3D sound field produced by the vibrating vessel sailing at an oblique angle of 45° to the $x = 0$ m axis at 200 Hz, with receiver depths of (a) $z = 2$ m, (b) $z = 20$ m, and (c) $z = 40$ m. See the supplementary material SuppPub3 for a complete video demonstrating the 3D sound field with different source orientations, with the yellow surface, near $y = 1$ km and $x = 4$ km, represents the topography.

reaches 90∘, a pronounced shadow zone appears along $y = 1$ km, caused by the trough of the radiation. A complete video demonstrating the 3D sound field generated by the ship at varying orientations is provided in the supplementary material.

4. Conclusions

In this article, we have derived a semi-analytical solution for 3D underwater acoustic propagation from a directional source within the framework of adiabatic normal modes. The derivation is based on the double-summation expression for the 3D sound field. The
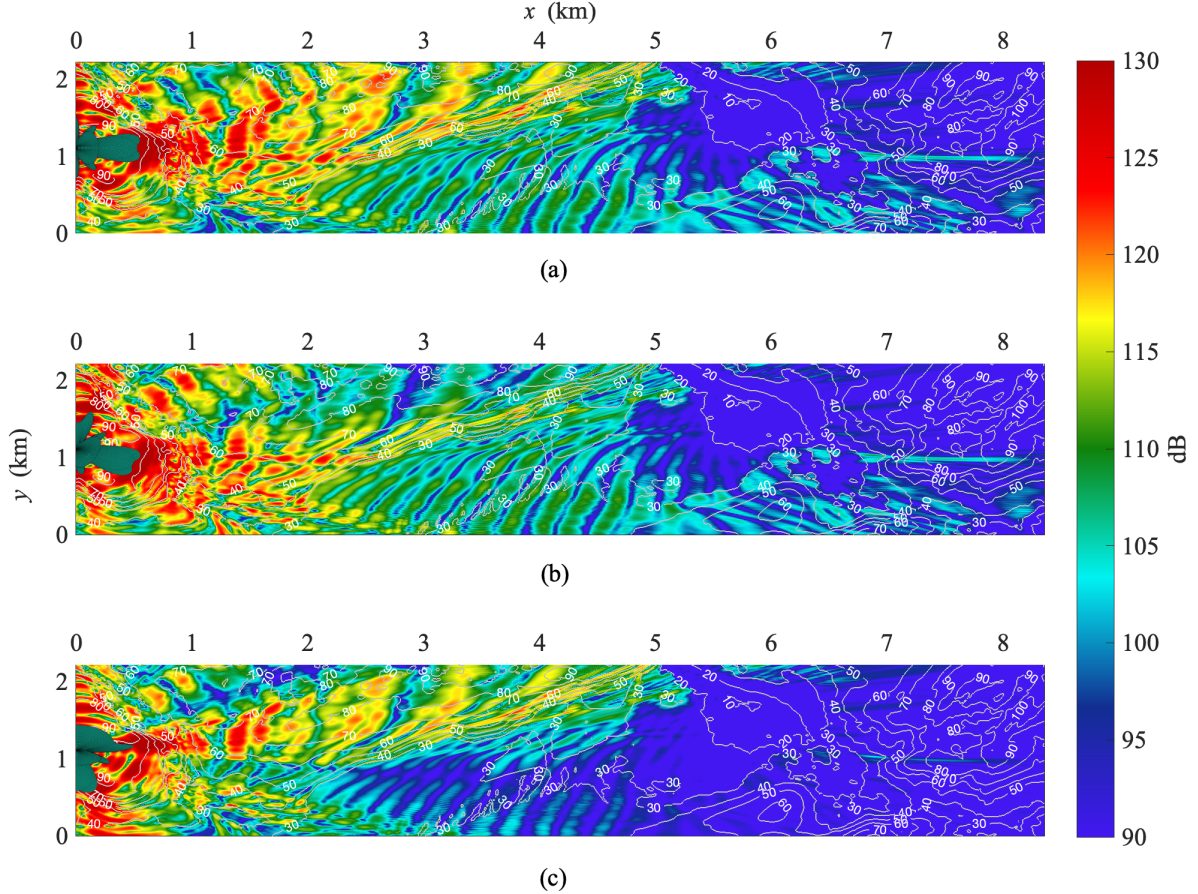
Figure 15: The 3D sound field generated by the vibrating vessel at $z = 30$ m with different orientation angles. The results are given for vessel orientations of (a) $\theta = 0\circ$, (b) $\theta = 20\circ$, and (c) $\theta = 90\circ$. See the supplementary material SuppPub3 for a complete video demonstrating the 3D sound field with different source orientations, with the yellow surface, near $y = 1$ km and $x = 4$ km, represents the topography.

Fraunhofer far-field approximation and two Taylor series expansions are used to simplify the source-strength integral representing directional radiation from a complex source. Two key assumptions are made: the depth derivative of the vertical wavenumber, k_{zj}, and the horizontal derivative of the wavenumber with respect to y, k_{yj}^{n}, are neglected. These assumptions are valid when the variations in the depth-dependent sound speed and the local topography where the source is imposed are small — conditions typically met in most practical scenarios [29].

The derived solution was validated through comparisons with an approach for predicting 3D structural acoustic radiation in range-independent waveguides. Two additional examples demonstrated the solution's effectiveness in addressing complex engineering problems. The results underscore the potential of this method for assessing the impact of shipping noise on marine fauna. Future work will incorporate modal interactions to further enhance the model's applicability.

Supplementary Material

See supplementary material at [URL will be inserted by publisher] for [See the supplementary material SuppPub1 for a complete video demonstrating the 3D sound field at different geotimes.]

See supplementary material at [URL will be inserted by publisher] for [See the supplementary material SuppPub2 for a complete video demonstrating the 3D sound field at different geotimes]

See supplementary material at [URL will be inserted by publisher] for [See the supplementary material SuppPub3 for a complete video demonstrating the 3D sound field with different source orientations, with the yellow surface, near $y = 1$ km and $x = 4$ km, represents the topography.]

Acknowledgments

Declaration of competing interest

The authors declare that they have no known competing financial interests or personal relationships that could have appeared to influence the work reported in this paper.

Data availability

No data was used for the research described in the article.

References

[1] M. S. Ballard, B. M. Goldsberry, M. J. Isakson, Normal mode analysis of three-dimensional propagation over a small-slope cosine shaped hill, J. Comput. Acoust. 23 (2015) 1550005. `doi:https://doi.org/10.1142/S0218396X15500058`.

[2] B. J. DeCourcy, T. F. Duda, A coupled mode model for omnidirectional three-dimensional underwater sound propagation, J. Acoust. Soc. Am. 148 (2020) 51–62. `doi:https://doi.org/10.1121/10.0001517`.

[3] R. de Moraes Calazan, O. C. Rodríguez, Simplex based three-dimensional eigenray search for underwater predictions, J. Acoust. Soc. Am. 143 (2018) 2059–2065. `doi:https://doi.org/10.1121/1.5030922`.

[4] M. B. Porter, Beam tracing for two-and three-dimensional problems in ocean acoustics, J. Acoust. Soc. Am. 146 (2019) 2016–2029. `doi:https://doi.org/10.1121/1.5125262`.

[5] R. N. Baer, Propagation through a three-dimensional eddy including effects on an array, J. Acoust. Soc. Am. 69 (1981) 70–75. `doi:https://doi.org/10.1121/1.385253`.

[6] Y.-T. Lin, T. F. Duda, A. E. Newhall, Three-dimensional sound propagation models using the parabolic-equation approximation and the split-step Fourier method, J. Comput. Acoust. 21 (2013) 1250018. `doi:https://doi.org/10.1142/S0218396X1250018X`.

[7] F. Sturm, Leading-order cross term correction of three-dimensional parabolic equation models, J. Acoust. Soc. Am. 139 (2016) 263–270. `doi:https://doi.org/10.1121/1.4939735`.

[8] K. Lee, W. Seong, Y. Na, Split-step Padé solver for three-dimensional Cartesian acoustic parabolic equation in stair-step representation of ocean environment, J. Acoust. Soc. Am. 146 (2019) 2050–2057. `doi:https://doi.org/10.1121/1.5125592`.

[9] K. Lee, W. Seong, Y. Na, Three-dimensional Cartesian parabolic equation model with higher-order cross-terms using operator splitting, rational filtering, and split-step Padé algorithm, J. Acoust. Soc. Am. 146 (2019) 2041–2049. `doi:https://doi.org/10.1121/1.5125428`.

[10] Y.-T. Lin, Three-dimensional boundary fitted parabolic-equation model of underwater sound propagation, J. Acoust. Soc. Am. 146 (2019) 2058–2067. `doi:https://doi.org/10.1121/1.5126011`.

[11] M. J. Isakson, N. P. Chotiros, Finite element modeling of acoustic scattering from fluid and elastic rough interfaces, IEEE J. Ocean. Eng. 40 (2014) 475–484. `doi:https://doi.org/10.1109/JOE.2014.2313060`.

[12] W. Liu, L. Zhang, W. Wang, Y. Wang, S. Ma, X. Cheng, W. Xiao, A three-dimensional finite difference model for ocean acoustic propagation and benchmarking for topographic effects, J. Acoust. Soc. Am. 150 (2021) 1140–1156. `doi:https://doi.org/10.1121/10.0005853`.

[13] A. Bottero, P. Cristini, D. Komatitsch, M. Asch, An axisymmetric time-domain spectral-element method for full-wave simulations: Application to ocean acoustics, J. Acoust. Soc. Am. 140 (2016) 3520–3530. `doi:https://doi.org/10.1121/1.4965964`.

[14] J. Lecoulant, T. C. Oliveira, Y.-T. Lin, Three-dimensional modeling of T-wave generation and propagation from a South Mid-Atlantic Ridge earthquake, J. Acoust. Soc. Am. 150 (2021) 3807–3824. `doi:https://doi.org/10.1121/10.0007072`.

[15] C. Li, B. K. Campbell, Y. Liu, D. K. Yue, A fast multi-layer boundary element method for direct numerical simulation of sound propagation in shallow water environments, J. Comput. Phys. 392 (2019) 694–712. doi:https://doi.org/10.1016/j.jcp.2019.04.068.

[16] T. He, S. Mo, E. Fang, M. Wang, R. Zhang, Modeling three-dimensional underwater acoustic propagation over multi-layered fluid seabeds using the equivalent source method, J. Acoust. Soc. Am. 150 (2021) 2854–2864. doi:https://doi.org/10.1121/10.0006663.

[17] P. S. Petrov, A. G. Tyshchenko, A. O. MacGillivray, Three-dimensional modelling of underwater noise produced by a bulk carrier vessel and estimation of its environmental impact, J. Acoust. Soc. Am. 155 (2024) 3702–3714. doi:https://doi.org/10.1121/10.0026238.

[18] G. H. Koopmann, L. Song, J. B. Fahnline, A method for computing acoustic fields based on the principle of wave superposition, J. Acoust. Soc. Am. 86 (1989) 2433–2438. doi:https://doi.org/10.1121/1.398450.

[19] M. Y. Trofimov, S. Kozitskiy, A. Zakharenko, A mode parabolic equation method in the case of the resonant mode interaction, Wave Motion. 58 (2015) 42–52. doi:https://doi.org/10.1016/j.wavemoti.2015.06.003.

[20] M. Y. Trofimov, A. D. Zakharenko, S. B. Kozitskiy, Mode Gaussian beam tracing, Comput. Phys. Commun. 207 (2016) 179–185. doi:https://doi.org/10.1016/j.cpc.2016.06.002.

[21] M. B. Porter, H. Bucker, Applications of Gaussian beam tracing to two and three-dimensional problems in ocean acoustics, Numerical and Applied Mathematics, JC Baltzer AG, Scientific Publising Co, 1989.

[22] M. E. Kelly, Z. Zou, L. Zhang, C. Shi, Ray tracing model for long-range acoustic vortex wave propagation underwater, Front. Acoust. 1 (2023) 1292050. doi:https://doi.org/10.3389/facou.2023.1292050.

[23] M. E. Kelly, C. Shi, Design and simulation of acoustic vortex wave arrays for long-range underwater communication, JASA Express Lett. 3 (2023). doi:https://doi.org/10.1121/10.0019884.

[24] Z. Fu, Q. Xi, Y. Li, H. Huang, T. Rabczuk, Hybrid FEM–SBM solver for structural vibration induced underwater acoustic radiation in shallow marine environment, Comput. Methods Appl. Mech. Eng. 369 (2020) 113236. doi:https://doi.org/10.1016/j.cma.2020.113236.

[25] L. W. Jiang, M. S. Zou, S. X. Liu, H. Huang, Calculation method of acoustic radiation for floating bodies in shallow sea considering complex ocean acoustic environments, J. Sound Vib. 476 (2020) 115330. doi:https://doi.org/10.1016/j.jsv.2020.115330.

[26] Q. Xi, Z. Fu, M.-A. Xue, M. Zou, J. Zheng, Analysis of underwater acoustic propagation induced by structural vibration in arctic ocean environment based on hybrid FEM-WSM solver, Ocean Eng. 287 (2023) 115922. doi:https://doi.org/10.1016/j.oceaneng.2023.115922.

[27] T. He, B. Wang, S. Mo, E. Fang, Predicting range-dependent underwater sound propagation from structural sources in shallow water using coupled finite element/equivalent source computations, Ocean Eng. 272 (2023) 113904. doi:https://doi.org/10.1016/j.oceaneng.2023.113904.

[28] T. He, X. Liu, R. Nie, W. Guo, S. Mo, B. Wang, Semi-analytical solution for sound propagation from a moving directional source in a shallow-water waveguide, J. Sound Vib. 576 (2024) 118259. doi:https://doi.org/10.1016/j.jsv.2024.118259.

[29] R. Nie, T. He, J. Fan, K. Zhao, B. Wang, Fast prediction of the long-range structural acoustic radiation in the stratified ocean, Ocean Eng. 314 (2024) 119673. doi:https://doi.org/10.1016/j.oceaneng.2024.119673.

[30] P. S. Petrov, M. Ehrhardt, A. G. Tyshchenko, P. N. Petrov, Wide-angle mode parabolic equations for the modelling of horizontal refraction in underwater acoustics and their numerical solution on unbounded domains, J. Sound Vib. 484 (2020) 115526. doi:https://doi.org/10.1016/j.jsv.2020.115526.

[31] A. G. Tyshchenko, M. A. Sorokin, S. B. Kozitskiy, P. S. Petrov, The solution of sound propagation modeling problems for environment impact assessment by the mode parabolic equations method, J. Acoust. Soc. Am. 156 (2024) 3306–3319. doi:https://doi.org/10.1121/10.0034424.

[32] T. He, J. Liu, S. Ye, X. Qing, S. Mo, A novel model order reduction technique for solving horizontal refraction equations in the modeling of three-dimensional underwater acoustic propagation, J. Sound Vib. 591 (2024) 118617. doi:https://doi.org/10.1016/j.jsv.2024.118617.

[33] F. B. Jensen, W. A. Kuperman, M. B. Porter, H. Schmidt, A. Tolstoy, Computational Ocean Acoustics, second ed., Springer-Verlag, New York, 2011.

[34] P. S. Petrov, M. Ehrhardt, S. B. Kozitskiy, A generalization of the split-step Padé method to the case of coupled acoustic modes equation in a 3D waveguide, J. Sound Vib. 577 (2024) 118304. `doi:https://doi.org/10.1016/j.jsv.2024.118304`.

[35] M. D. Collins, The adiabatic mode parabolic equation, J. Acoust. Soc. Am. 94 (1993) 2269–2278. `doi:https://doi.org/10.1121/1.407498`.

[36] A. T. Abawi, W. A. Kuperman, M. D. Collins, The coupled mode parabolic equation, J. Acoust. Soc. Am. 102 (1997) 233–238. `doi:https://doi.org/10.1121/1.419819`.

[37] W. Men, L. Zhang, J.-W. Yin, X. Han, H.-Y. Yin, Blind beamforming-based strong interference suppression in underwater acoustic direct-sequence code-division multiple-access systems, J. Acoust. Soc. Am. 152 (2022) 2128–2139. `doi:https://doi.org/10.1121/10.0014598`.

[38] R. Kirby, Atmospheric sound propagation in a stratified moving media: Application of the semi analytic finite element method, J. Acoust. Soc. Am. 148 (2020) 3737–3750. `doi:https://doi.org/10.1121/10.0002912`.

[39] R. Kirby, Atmospheric sound propagation in a moving fluid above an impedance plane: Application of the semi-analytic finite element method, J. Acoust. Soc. Am. 149 (2021) 1285–1295. `doi:https://doi.org/10.1121/10.0003567`.

[40] D. R. Barclay, Y.-T. Lin, Three-dimensional ambient noise modeling in a submarine canyon, J. Acoust. Soc. Am. 146 (2019) 1956–1967. `doi:https://doi.org/10.1121/1.5125589`.

[41] T. C. Oliveira, Y.-T. Lin, M. B. Porter, Underwater sound propagation modeling in a complex shallow water environment, Front. Mar. Sci. 8 (2021) 751327. `doi:https://doi.org/10.3389/fmars.2021.751327`.

[42] J. R. Apel, M. Badiey, C.-S. Chiu, S. Finette, R. Headrick, J. Kemp, J. F. Lynch, A. Newhall, M. H. Orr, B. H. Pasewark, et al., An overview of the 1995 swarm shallow-water internal wave acoustic scattering experiment, IEEE J. Ocean. Eng. 22 (3) (1997) 465–500. `doi:https://doi.org/10.1109/48.611138`.

[43] B. W. Eakins, Digital elevation model of Montauk, New York procedures, data sources and analysis, National Geophysical Data Center, Marine Geology and Geophysics Division, 2009. `https://repository.library.noaa.gov/view/noaa/13415`.

[44] R. H. Headrick, J. F. Lynch, J. N. Kemp, A. E. Newhall, K. von der Heydt, J. Apel, M. Badiey, C.-s. Chiu, S. Finette, M. Orr, et al., Acoustic normal mode fluctuation statistics in the 1995 SWARM internal wave scattering experiment, J. Acoust. Soc. Am. 107 (2000) 201–220. `doi:https://doi.org/10.1121/1.428563`.

[45] M. Badiey, B. G. Katsnelson, J. F. Lynch, S. Pereselkov, W. L. Siegmann, Measurement and modeling of three-dimensional sound intensity variations due to shallow-water internal waves, J. Acoust. Soc. Am. 117 (2005) 613–625. `doi:https://doi.org/10.1121/1.1828571`.

[46] C. Li, An efficient multi-layer boundary element method for direct computation of sound propagation in shallow water environments, PhD Thesis, Massachusetts Institute of Technology, 2019.

[47] M. J. Isakson, N. P. Chotiros, Finite element modeling of reverberation and transmission loss in shallow water waveguides with rough boundaries, J. Acoust. Soc. Am. 129 (2011) 1273–1279. `doi:https://doi.org/10.1121/1.3531810`.

[48] M. A. Ainslie, Principles of Sonar Performance Modelling, Springer-Verlag, Berlin, 2010.